

## KECK/HIRES SPECTROSCOPY OF V838 MONOCEROTIS IN OCTOBER 2005\*

T. KAMIŃSKI<sup>1</sup>, M. SCHMIDT<sup>1</sup>, R. TYLEND<sup>1</sup>, M. KONACKI<sup>1,2</sup>, AND M. GROMADZKI<sup>1</sup>

ACCEPTED TO APJS: February 12, 2009

### ABSTRACT

V838 Mon erupted at the beginning of 2002 becoming an extremely luminous star with  $L \simeq 10^6 L_{\odot}$ . Among various scenarios proposed to explain the nature of the outburst the most promising is a stellar merger event. In this paper we investigate the observational properties of the star and its surroundings in the post outburst phase. We have obtained a high resolution optical spectrum of V838 Mon in October 2005 using the Keck I telescope. We have identified numerous atomic features and molecular bands present in the spectrum and provided an atlas of those features. In order to improve the spectrum interpretation we have performed simple modeling of the molecular bands. Our analysis indicates that the spectrum is dominated by molecular absorption features arising in photospheric regions with temperatures of  $\sim 2400$  K and in colder outer layers, where the temperature decreases to  $\sim 500$  K. A number of resonance lines of neutral alkali metals are observed to show P-Cyg profiles. Particularly interesting are numerous prominent emission lines of [Fe II]. All of them show practically the same profile, which can be well described by a Lorentzian profile. In the blue part of the spectrum photospheric signatures of the B-type companion are easily seen. We have fitted the observed spectrum with a synthetic one and the obtained parameters are consistent with the B3V type. We have also estimated radial and rotational velocities of the companion.

*Subject headings:* binaries: spectroscopic — stars: emission-line — stars: individual (V838 Mon) — stars: mass loss — stars: winds, outflows — stars: variables: other

### 1. INTRODUCTION

The eruption of V838 Mon was discovered in the beginning of January 2002. Initially thought to be a nova, the object appeared unusual and enigmatic in its nature. The eruption, as observed in the optical, lasted about three months (Munari et al. 2002b; Kimeswenger et al. 2002; Crause et al. 2003). After developing an A-F supergiant spectrum at the maximum at the beginning of February 2002, the object evolved to lower effective temperatures and in April 2002 it practically disappeared from the optical, remaining very bright in the infrared. At the same time a B3V companion to the erupted object was discovered in the optical (Munari et al. 2002a). A detailed analysis of the evolution of the object in the outburst and decline can be found, e.g. in Tyrenda (2005).

Several mechanisms have been proposed to explain the eruption of V838 Mon, including an unusual nova (Iben & Tutukov 1992), a late He-shell flash (Lawlor 2005), and a stellar merger (Soker & Tyrenda 2003). They have critically been discussed in Tyrenda & Soker (2006). These authors conclude that the only mechanism that can satisfactorily account for the observational data is a collision and merger of a low-mass pre-main-sequence star with a  $\sim 8 M_{\odot}$  main-sequence star.

In October/November 2006 the B3V companion sig-

nificantly faded and a strong H $\alpha$  emission appeared in the spectrum of V838 Mon (Goranskij 2006; Bond 2006). Late in 2004 an emission-line spectrum, composed mainly of [Fe II] lines, started to develop (Barsukova et al. 2006), reaching its maximum around the 2006 eclipse-like event (Munari et al. 2007).

In the present paper we present and discuss a high resolution spectrum of V838 Mon acquired with the Keck I telescope in October 2005. At that time the [Fe II] emission-line spectrum was already well developed and the object was a year before the eclipse of the B3V companion.

### 2. OBSERVATIONS AND DATA REDUCTION

A high resolution spectrum of V838 Mon was obtained on 2005 October 13 UT with the High Resolution Echelle Spectrometer (HIRES, Vogt et al. 1994) attached to the Keck I telescope. We used the C4 decker, which provides a slit with dimensions  $1''148 \times 3''5$ . The resultant resolving power was of  $R \simeq 34000$ . The HIRES instrument makes use of a 3-chip mosaic as a detector. We obtained two exposures of the object with a total time of 960 s.

Data reduction was performed with the IRAF<sup>4</sup> standard procedures (Massey 1997). Data were debiased and flat-fielded using the *ccdproc* task. Cosmic ray events were removed from the CCD frames with a method described in van Dokkum (2001). After a careful check of the removal we are confident that the procedure did not introduce any spurious effects to the spectra. Order tracing and extraction were done using the tasks in

<sup>4</sup> IRAF is distributed by the National Optical Astronomy Observatories, which are operated by the Association of Universities for Research in Astronomy, Inc., under cooperative agreement with the National Science Foundation.

Electronic address: tomkam@ncac.torun.pl

\* The data presented herein were obtained at the W.M. Keck Observatory, which is operated as a scientific partnership among the California Institute of Technology, the University of California and the National Aeronautics and Space Administration. The Observatory was made possible by the generous financial support of the W.M. Keck Foundation.

<sup>1</sup> Department of Astrophysics, Nicolaus Copernicus Astronomical Center, Radańska 8, 87-100 Toruń, Poland

<sup>2</sup> Astronomical Observatory, A. Mickiewicz University, Słoneczna 36, 60-286 Poznań, Poland

the *echelle* package. The orders corresponding to the bluest part of the spectra were underexposed and we were not able to extract them, even with a pinhole trace as a reference. The wavelength calibration was based on ThAr lamp observations and it is accurate to within  $0.003 \text{ \AA}$ . The two extracted echelle spectra were averaged giving a spectrum with a total wavelength coverage  $3720 - 7962 \text{ \AA}$ . In the range there are, however, numerous gaps caused by the inter-chip spaces on the mosaic and the orders that do not overlap.

Using an extracted pinhole frame we corrected all the orders of the echelle spectrum for a blaze effect. Inspection of the overlapping and blaze-corrected orders revealed that, although correctly flattened, they were systematically tilted in such a way that the long-wavelength end of an order was always higher on a relative intensity scale than the short-wavelength end of the neighboring order. The discrepancy was of 15% of the average intensity of the order. We reduced the tilt by multiplying each order by a linear function (i.e. with 1 in the middle of an order range, and  $1 \pm 0.075$  at the edges). All the overlapping orders were then safely merged and, subsequently, we got a spectrum composed of three parts: (i) completely covered wavelength range over  $3720 - 4883 \text{ \AA}$ , (ii) wide range over  $4951 - 6469 \text{ \AA}$  with two narrow gaps at  $6308.5 - 6310 \text{ \AA}$  and  $6401 - 6424.5 \text{ \AA}$ , and (iii) a part of the spectrum over the range  $6544 - 7962 \text{ \AA}$  with 10 non-overlapping orders. The three pieces we call hereafter parts blue, green and red, respectively.

Since no spectrophotometric standard stars were observed during our observing run at Keck I, we decided to flux calibrate the HIRES spectrum on a base of the method described in Suzuki et al. (2001), namely by using a flux calibrated spectrum of V838 Mon obtained elsewhere with a lower spectral resolution. Such a low resolution spectrum was acquired on 2005 November 22 with the Grating Spectrograph with SITe mounted at the 1.9 m Radcliffe telescope at the South African Astronomical Observatory (SAAO). We made use of a grating #7 with 300 lines  $\text{mm}^{-1}$ , and a slit with a projected width  $1''.5$ . The last figure was comparable to seeing conditions during the observation ( $\sim 1''.4$ ). The total duration of the exposure was 1000 s. Three spectrophotometric standard stars, i.e. LTT9239, EG21, and LTT3218, were observed during the night. This allowed us to calibrate the low resolution spectrum in absolute flux units, while the wavelength calibration was performed with ThAr reference lamp spectra. All the data reduction and calibrations were carried out with standard IRAF procedures. The extracted and flux calibrated spectrum covers the range  $3817 - 7235 \text{ \AA}$  with a resolving power of  $R \simeq 1000$ .

The flux calibration of the HIRES spectrum was performed as follows. The high and low resolution spectra were corrected to the heliocentric rest frame and they were cross-correlated in order to find a relative shift between them in the wavelength domain. We found a shift of  $5.5 \text{ \AA}$  (note that the value is close to the spectral resolution in the SAAO observations), which was eliminated by displacing the low resolution spectrum. Next, the HIRES spectrum was smoothed to the resolution of the observations at SAAO and the spectra were divided one by the other. Rather than to calibrate each single order

of the echelle spectrum, as it was done in Suzuki et al. (2001), we decided to calibrate separately only the three mentioned above parts of the merged spectrum. To each of the pieces a low order polynomial was fitted giving a conversion ratio (CR, cf. Suzuki et al. 2001). Since the SAAO spectrum has a narrower wavelength range than the high resolution one, we extrapolated the CRs to the full ranges of the blue and red parts. Finally, the HIRES spectrum was put on the absolute flux scale by dividing its parts by the appropriate CRs. We note that the flux calibration of our final spectrum is uncertain, particularly in the ranges not covered by the SAAO observations and in the regions where strong atmospheric molecular bands are present (the object was observed at unequal air masses in the different facilities).

Although the low resolution spectrum was obtained about six weeks after the HIRES observations, we are quite confident that the spectrum of V838 Mon did not change significantly during this period in the observed spectral range. A comparison of the spectra smoothed to the same resolution shows that there are no significant discrepancies which would affect the flux calibration. Moreover, from the photometric behavior of the object, illustrated e.g. on the V. Goranskij's web page<sup>5</sup>, one can see that the assumption of a constant flux in B and V bands during the period is justified.

The flux calibrated spectrum was then corrected for the interstellar reddening using the IRAF's task *deredden* with  $E_{B-V} = 0.90$  (Tylanda 2005) and with a standard ratio of total to selective extinction  $R_V = 3.1$ .

### 3. THE SPECTRUM

The flux-calibrated and dereddened spectrum of V838 Mon is presented in Figs. 1–3. For a comparison a synthetic spectrum of a B-type star (see Sect. 6) is overplotted with the blue line. Most of identified atomic and molecular features are indicated in the figures. Wavelengths are given in the heliocentric rest frame and the units of the flux are  $10^{-13} \text{ erg s}^{-1} \text{ cm}^{-2} \text{ \AA}^{-1}$ .

Our observations reveal an unusual and very complex spectrum of V838 Mon. It contains contributions from several physically different environments. In its blue part a photospheric spectrum of the B3V companion can be clearly seen, while the green and red parts are dominated by molecular absorptions that severely affect the flux of a very cold supergiant. A particularly striking feature of the presented spectrum is the presence of prominent emissions of [Fe II]. Finally numerous, mostly resonance, lines showing P-Cyg profiles as well as a few pure absorptions of neutral atoms can be easily found.

In the case of such a complex spectrum, detailed identification of all the features is a difficult task. The identification procedures and their results are described in the following sections. We also present results of basic measurements, e.g. radial velocities of different line systems and molecular bands.

### 4. ATOMIC LINES

The atomic line identification was based mainly on the Atomic Spectra Database Lines Form<sup>6</sup> (provided by the National Institute of Standards and Technology, NIST),

<sup>5</sup> <http://jet.sao.ru/~goray/v838mon.htm>

<sup>6</sup> [http://physics.nist.gov/PhysRefData/ASD/lines\\_form.html](http://physics.nist.gov/PhysRefData/ASD/lines_form.html)

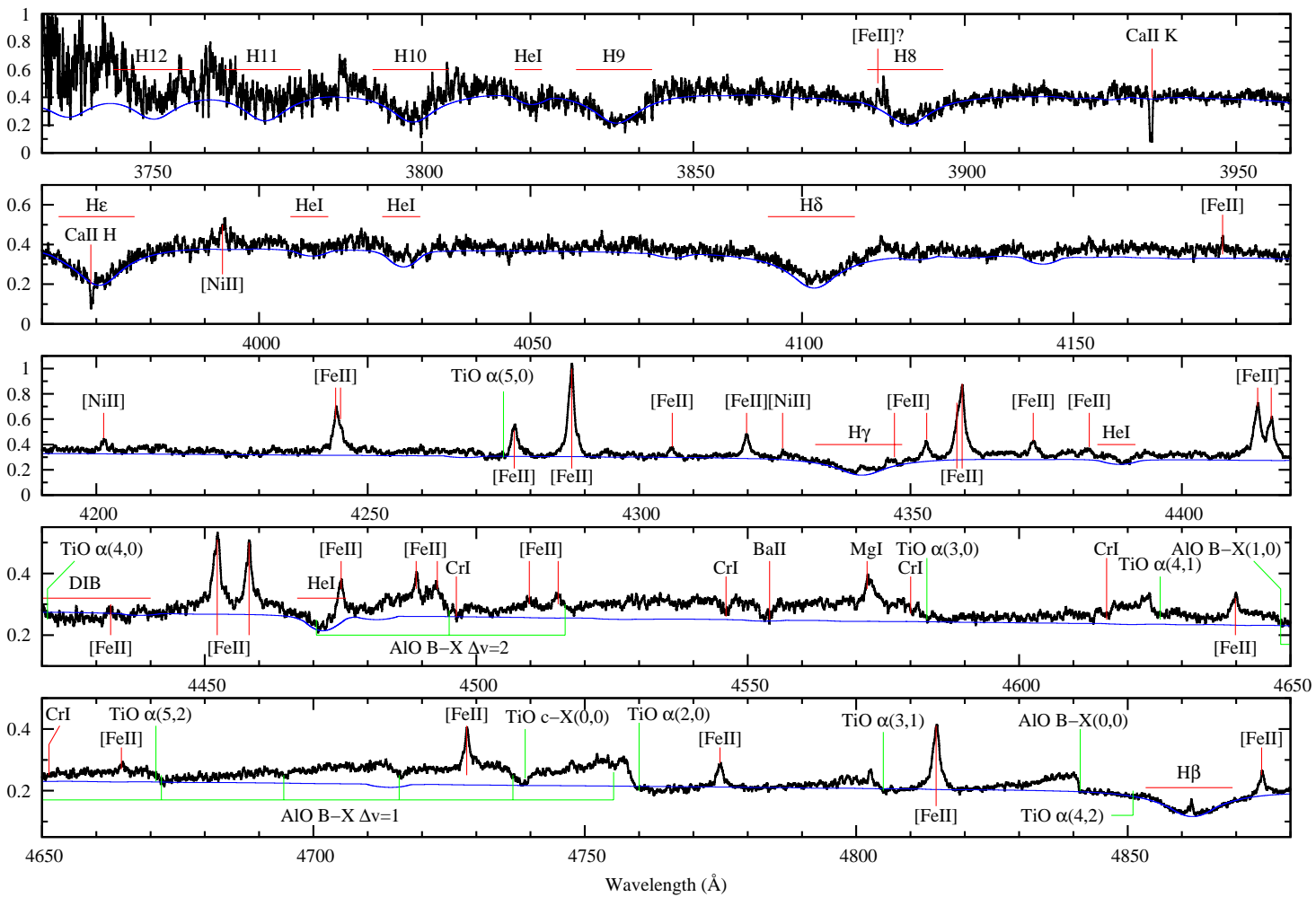


Fig. 1. — Blue part of the Keck spectrum of V838 Mon obtained in October 2005. The spectrum was smoothed from the original resolution with boxcar 13. A synthetic spectrum of a B3V star is shown for comparison (blue line). Identified atomic spectral features are indicated by red markers, while molecular bandheads are assigned with green markers. The ordinate units are  $10^{-13} \text{ erg s}^{-1} \text{ \AA}^{-1}$ .

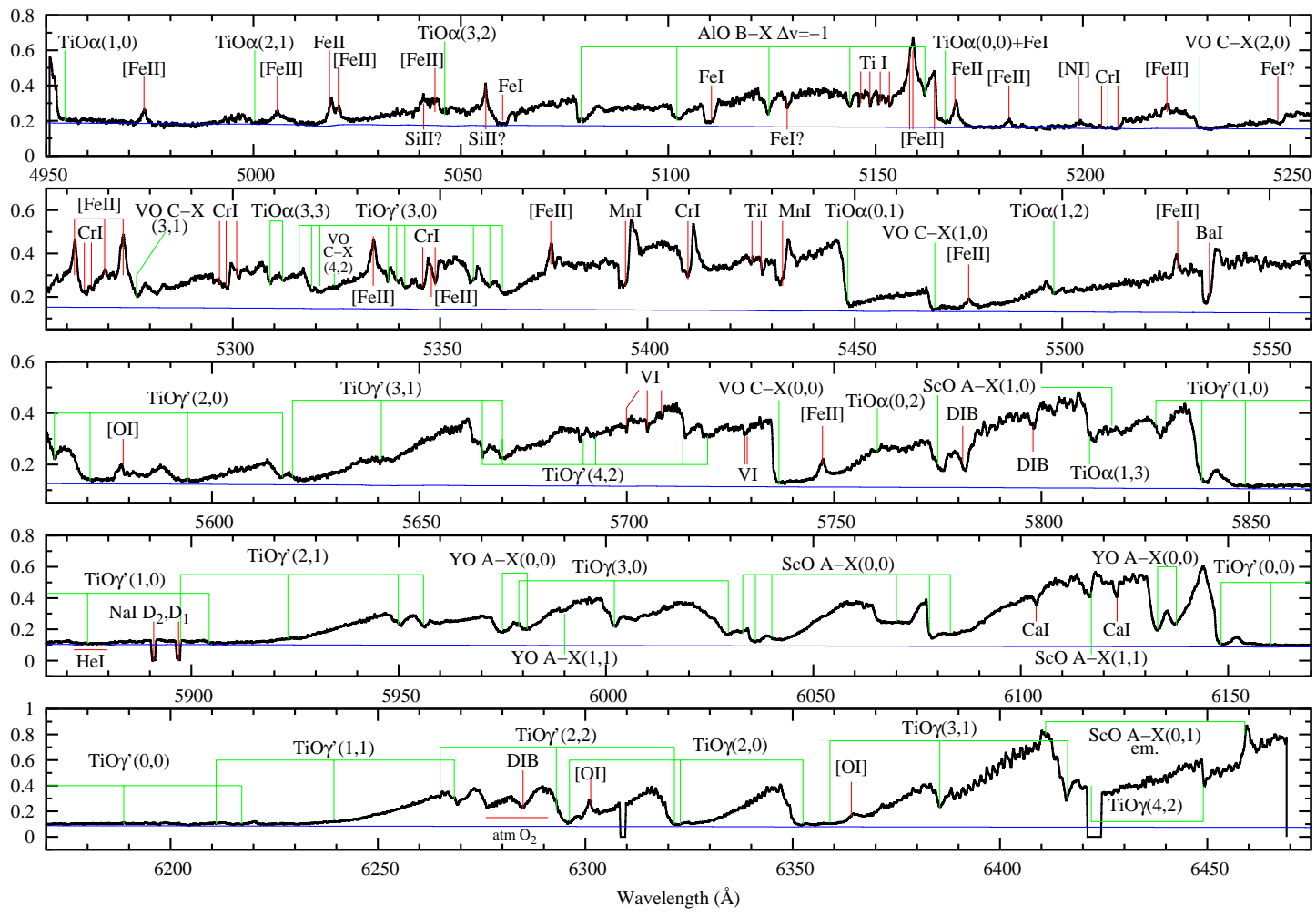


FIG. 2.— Same as in Fig. 1 but for the green part of the Keck spectrum of V838 Mon.

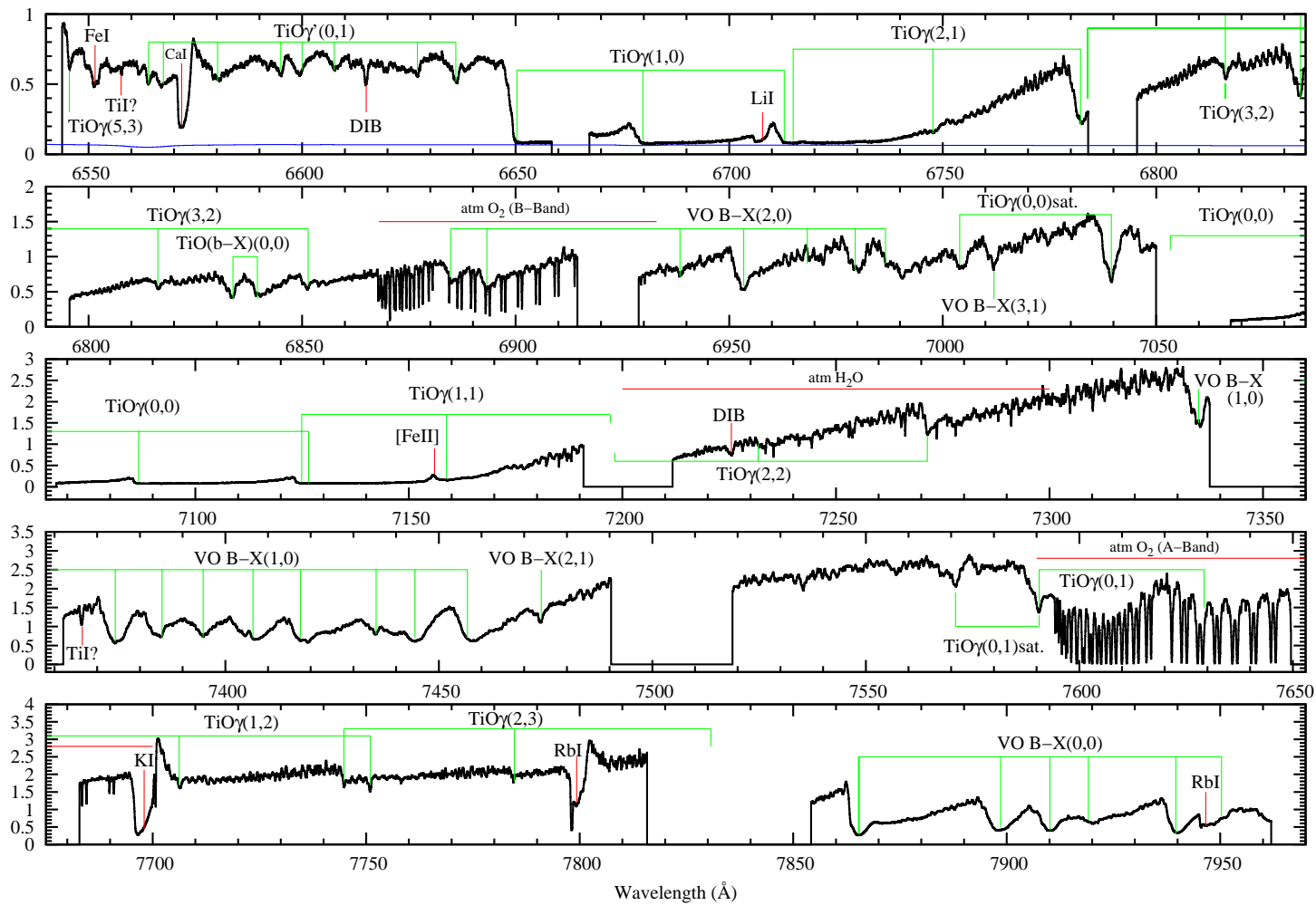


FIG. 3.— Same as in Fig. 1 but for the red part of the Keck spectrum of V838 Mon.

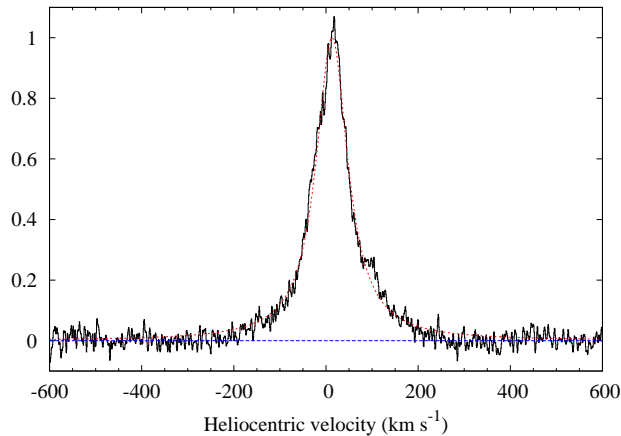


FIG. 4.— Profile of the [Fe II] lines. *Black solid line*: the profile averaged out from 7 lines (see the text for more details). *Red dotted line*: the best least-squares fit of a Lorentzian profile to the average profile (FWHM of  $83.6 \text{ km s}^{-1}$ , center at  $13.0 \text{ km s}^{-1}$ ). *Blue dashed line*: local continuum.

the Atomic Line List version 2.04 by van Hoof<sup>7</sup>, and on the multiplet tables by Moore (1945).

All the identified atomic emission and absorption features are listed in Tables 1 and 2 (respectively) in order of their laboratory wavelengths. Columns (1)–(3) of the tables contain: laboratory wavelength, ion name, and multiplet number from Moore (1945). Column (4) in Table 1 gives integrated (dereddened) fluxes of the emission lines (for which a reliable measurement was possible). In the same column of Table 2 the profile type (pure absorption or P-Cyg) is specified. Notes on the features are given in the last column of the tables.

#### 4.1. Emission lines

##### 4.1.1. Forbidden lines

A great majority of the emission features seen in the spectrum are forbidden lines of Fe II. They are remarkably numerous. We have identified 49 lines from 11 different multiplets. All of them arise from levels with energies (above the ground level) between 2.0 and 3.4 eV. Most of them are very strong and often blended with other spectral features. In addition to these forbidden transitions, we have also found two permitted lines of Fe II at 5018 Å and 5169 Å (a third line from the same multiplet falls in a gap between two chips).

All the unblended [Fe II] emissions show practically the same but rather unusual shape. It can be well fitted with a theoretical Lorentzian profile, as can be seen from Fig. 4. The profile shown in this figure is a mean shape obtained from seven strongest and “clean” [Fe II] lines. When averaging, the normalized profiles of individual lines were weighted according to the rms<sup>2</sup> values of the local noise in the spectrum. From 30 [Fe II] lines, for which we successfully fitted a Lorentzian profile using IRAF’s *splot*, we have obtained a typical full width at half maximum<sup>8</sup> (FWHM) of  $76.3 \pm 17.7 \text{ km s}^{-1}$  (median and standard deviation). All the lines have practically the same radial velocity. Measurements performed with the

<sup>7</sup> <http://www.pa.uky.edu/~peter/atomic/>

<sup>8</sup> All line widths given in this paper are not corrected for the instrumental profile, which has an intrinsic width of about  $9 \text{ km s}^{-1}$ .

IRAF’s *rvdlines* task gave a heliocentric radial velocity of  $V_h = 13.3 \pm 0.7 \text{ km s}^{-1}$  (mean and standard deviation).

Other forbidden lines seen in our spectrum include those of [O I] 5577 Å, 6300 Å, 6364 Å and [N I] 5198 Å. These are rather weak features, observed in spectral regions strongly contaminated with molecular bands. Their measurements are therefore uncertain. The measured FWHM and radial velocity of the [O I] lines are  $80 \pm 30 \text{ km s}^{-1}$  and  $40 \pm 10 \text{ km s}^{-1}$ , respectively. The [N I] line has a radial velocity of about  $80 \text{ km s}^{-1}$ .

It should be noted that some of the emission lines listed in Table 1 have uncertain identification. Two strong features at about 5041 Å and 5056 Å were identified as Si II, but other identifications are possible. Three lines recognized as [Ni II] 3993 Å, 4201 Å, and 4326 Å, are weak, which makes their identification uncertain. However, the ionization potential of Si and Ni being similar to that of Fe and low excitation energies of the proposed multiplets make the identification probable.

##### 4.1.2. Balmer lines

Inside the cores of the photospheric Balmer lines of the B-type companion weak emission features can be found. Their presence is evident when one compares the observed photospheric profiles with a synthetic spectrum of an early B-type star (see Fig. 1). The following discussion is limited to H $\beta$  only, as the emission feature is most evident in this line. In order to better characterize the emission we have subtracted the underlying stellar absorption. The procedure was as follows. To the wings of the absorption line we fitted a profile in the form:

$$\phi(\lambda) = d \exp\{-[a(\lambda \pm \lambda_c)^b + c]^{-1}\} \quad (1)$$

with  $a$ ,  $b$ ,  $c$  and  $d$  as free parameters. The central wavelength,  $\lambda_c$ , was taken as the laboratory wavelength of the H $\beta$  line corrected for the radial velocity of the B3V star (see Sect. 6). Eq. (1) is based on an empirical profile given in Chauville et al. (2001). However, for our purpose it was generalized to treat also the local continuum level as a free parameter. The fitting procedure used the least-squares method and it was applied to all the data points in the H $\beta$  wing [i.e., not only to three points, as in Chauville et al. (2001)]. The core region dominated by emissions was, obviously, excluded from the fit. The extracted emission feature is shown in Fig. 5. It can be interpreted as a single emission with an absorption superimposed on it. In this case, fitting Lorentzian profiles gives the emission component with a FWHM of  $\sim 42 \text{ km s}^{-1}$  at a radial velocity of  $\sim 14 \text{ km s}^{-1}$ , while the absorption component appears at  $\sim 10 \text{ km s}^{-1}$  and has a FWHM of  $\sim 24 \text{ km s}^{-1}$ . Note that the parameters of the emission component in this case are close to those of the [Fe II] lines. Alternatively, if the observed profile is fitted with two emission components, they have radial velocities of  $\sim -10$  and  $\sim 28.8 \text{ km s}^{-1}$ , and FWHMs of  $\sim 30$  and  $\sim 24 \text{ km s}^{-1}$ , respectively.

##### 4.2. P-Cyg features

The spectrum displays a number of strong resonance lines showing P-Cyg profiles. The most prominent ones are those of Mn I 5395 Å and 5433 Å, Cr I 5410 Å, Ba I 5535 Å, Ca I 6573 Å, K I 7699 Å, Rb I 7800 Å (only

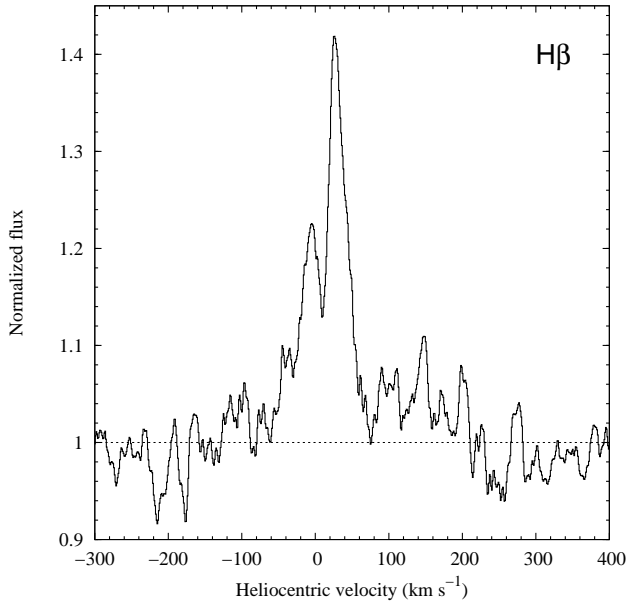


FIG. 5.— Emission feature extracted from the  $H\beta$  photospheric absorption line of the B3V companion. The spectrum was significantly smoothed from the original resolution via boxcar with a box size of 15 pixel.

the Cr I line is not a resonant one). They are shown in Fig. 6. Other lines showing P-Cyg signatures, although not as notable as in those listed above, are Mg I 4571 Å, Fe I 5110 Å, and possibly also a few weak lines of Cr I.

Most of the P-Cyg profiles have a deep absorption component extending from  $\sim 50$  km s $^{-1}$  (as a cross-over from emission to absorption) to  $\sim -95$  km s $^{-1}$ . The most extreme exception is the K I line, which shows blueshifted absorption down to  $\sim -145$  km s $^{-1}$ . Emission components peak at  $\sim 80$  km s $^{-1}$ .

The shapes of the absorption components indicate inhomogeneities in the outflowing matter. Particularly in the profiles of Rb I and Mn I one can clearly see an additional narrow absorption component (NAC) centered at  $-82$  km s $^{-1}$  [see panel (b) in Fig. 6]. The measured FWHM of the narrow feature inside the Rb I 7800 Å line is 19.3 km s $^{-1}$ .

As noted above, the Mg I 4571 Å line shows only weak signatures of a P-Cyg profile. Indeed, it is dominated by a slightly asymmetric emission and exhibits only a very weak absorption at approximately the same velocity as the NAC.

The profile of Fe I 5110 Å is also exceptional. Its absorption component is so deep that it removes all the light from the cold star and reaches the flux level of the B3V companion (see top panel in Fig. 2). In addition, it is considerably broader than most of the other P-Cyg absorptions and extends from  $\sim 80$  km s $^{-1}$  to  $\sim -120$  km s $^{-1}$ . Most probably the  $\lambda 5110$  absorption is saturated. Other Fe I lines identified in the spectrum appear as absorptions only, without any signs of emission components (see Sect. 4.3).

As Table 2 indicates, almost all the abundant alkali metals show P-Cyg profiles. Thus, one would expect that it should also be the case of the Li I doublet at 6708 Å. However, in the raw spectrum no clear emission component can be seen close to the clear absorption of

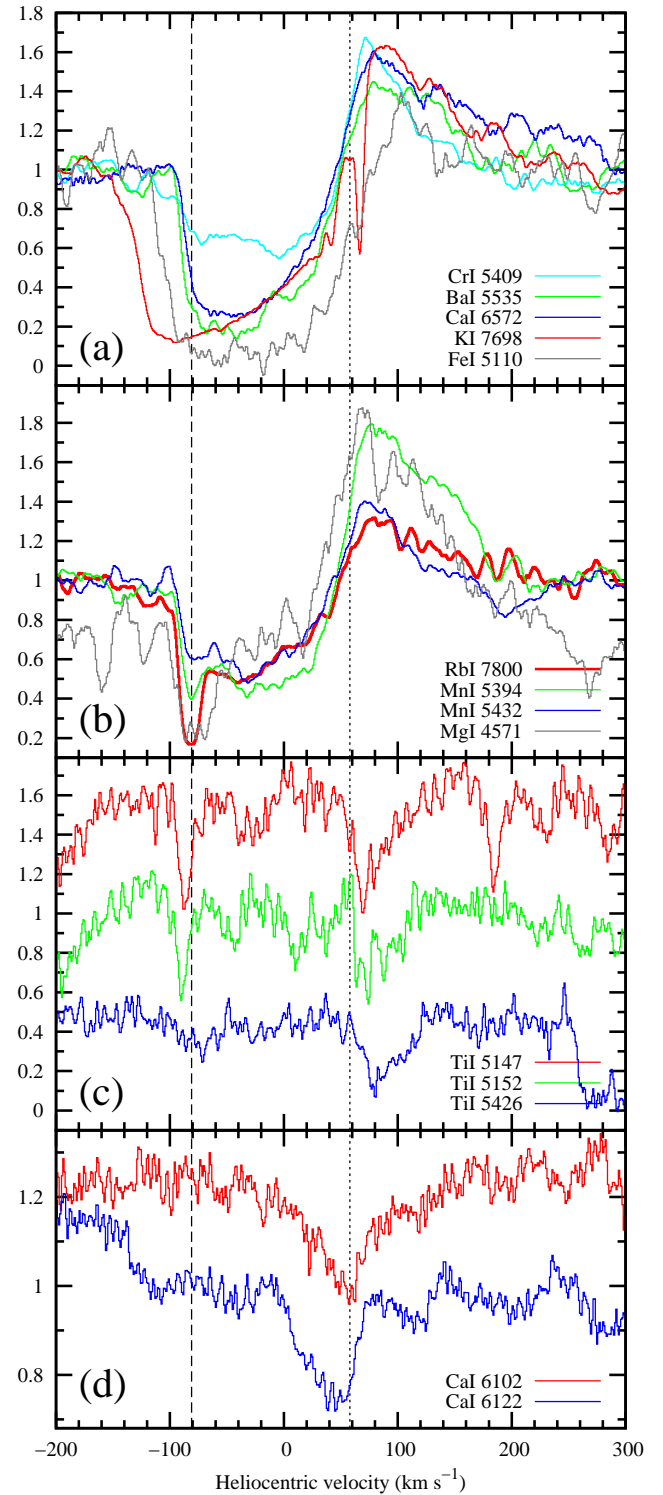


FIG. 6.— Sample of atomic spectral features. Before the regions were individually normalized to the local continuum, the flux from the B3V star had been subtracted. (a) Examples of the most prominent P-Cyg lines. The spectra of Cr I, Ba I and Fe I, were smoothed via boxcar 9. The K I profile is contaminated by the ISM absorptions. (b) P-Cyg profiles with a narrow absorption component (NAC). The normalized fluxes of the Mg I were divided by 1.7 and the spectrum was smoothed via boxcar 13. The Mn I lines were smoothed with boxcar 9. (c) Double absorption components of three Ti I transitions; the upper and lower plots were vertically shifted by  $\pm 0.55$ . (d) Two absorption lines of Ca I. The vertical lines along the panels mark the velocity of the NAC (dashed) and of the source of the outflow (dotted) as estimated from molecular bands (see Sect. 5.1).



Li I. The doublet falls in a region that is dominated by a strong absorption band of TiO and it is difficult to define an underlying molecular baseline. Moreover, the doublet resides very close to the  $\gamma$  (1,0) bandhead of TiO and most probably a part of the emission component of Li I is absorbed by the saturated molecular band. A similar situation also occurs for the Rb I 7948 Å line. Its profile is strongly affected by the (B–X) (0,0) absorption band of VO and the expected emission component cannot be seen on the raw spectrogram.

#### 4.3. Absorption lines

Another group of identified lines are pure absorptions. Beside the interstellar features (see Sect. 7) and photospheric lines of a B-type star (see Sect. 6), absorptions of Fe I 5060 Å, 5128 Å, 5247 Å, 6551 Å, Ca I 6102 Å and 6122 Å, and numerous Cr I lines were found. Some of these lines are in the same multiplet with a line that exhibits a prominent P-Cyg profile. Thus, it is quite possible that in a more sensitive observations the lines, classified here as absorptions, would appear as P-Cyg profiles. Among the absorptions the strongest is the Fe I 5060 Å line, which, similarly to the P-Cyg absorption component of Fe I at 5110 Å (see Sect. 4.2), appears as a very broad feature and, probably, is saturated. All the absorptions, except the  $\lambda$ 5060 line, are narrower than the absorption components in the P-Cyg profiles and always fall in the velocity range defined by P-Cyg absorptions, indicating that they originate in the same parts of the outflowing gas.

The absorption lines of Ti I found at 5147 Å, 5152 Å, and 5426 Å are of special interest. They arise from levels with energies of 2.3–2.4 eV. In our spectrum the lines consist of (at least) two well separated components, what is clearly seen in panel (c) of Fig. 6. The redshifted absorption component appears at  $\sim 75$  km s<sup>-1</sup>, close to the peaks in the P-Cyg emissions. The blueshifted sharp feature, seen in the 5147 Å and 5152 Å lines, appears at a radial velocity of  $\sim -90$  km s<sup>-1</sup>, which suggests that it can be associated with portions of the fast wind seen in the most blueshifted P-Cyg absorptions (excluding K I). Note also that the velocity of this short-wavelength component is also very close to the velocity of the NAC seen in some P-Cyg profiles (see Fig. 6). As can be seen from panel (c) in Fig. 6, the two absorption components of the Ti I lines have different shapes. While the blueshifted component has a very narrow Gaussian profile with a FWHM of  $\sim 13$  km s<sup>-1</sup>, the redshifted feature is broad, with a FWHM of  $\sim 40$  km s<sup>-1</sup>, and its profile is asymmetric with a steep blue edge and an extended red wing.

A prominent absorption feature is present at  $\sim 7366$  Å, which we have identified as another Ti I line at 7364 Å. The feature would correspond to the blueshifted component in the discussed above Ti I lines. Note that the feature has also a profile similar to the corresponding absorptions in the other Ti I lines. A possible redshifted component cannot be seen, because it falls in a region between the echelle orders.

We have also identified two weak absorption lines of Ca I at 6103 Å and 6122 Å. They are shown in panel (d) of Fig. 6. These lines are broad (FWHM  $\simeq 60$  km s<sup>-1</sup>) and asymmetric. Contrary to the Ti I lines, they have

an extended blue wing and a sharp red edge. Since these Ca I lines arise from a rather high energy level (3.91 eV above the ground level), they are expected to be formed close to the photosphere of the red supergiant.

## 5. MOLECULAR BANDS

The complexity of the spectrum makes a direct identification of molecular bands very difficult. For identification purposes, we have performed a series of simulations of molecular spectra. First attempts showed that a model capable of reasonably reproducing the observed molecular features should include, at least, two components, i.e., a stellar photosphere of a cool supergiant and an absorbing outflowing material with an excitation temperature significantly lower than the stellar temperature.

As a model of the stellar cold photosphere, we have used a synthetic spectrum generated from a model atmosphere from the NextGen grid<sup>9</sup> (Hauschildt et al. 1999). These models include TiO opacities, what is crucial in the case of the analyzed spectrum. We chose a model atmosphere with  $T_{\text{eff}} = 2400$  K, and with the lowest gravity available within the grid, i.e.  $\log g = 0.0$ . For these parameters there is only a NextGen model with solar metallicity, what is probably close to the true metallicity of V838 Mon (Kipper & Škoda 2007).

Our choice on  $T_{\text{eff}}$  is a result of initial modeling of the observed spectrum, where we used atmosphere models for  $T_{\text{eff}} = 2000, 2200,$  and  $2400$  K. With the value of 2400 K we have obtained most satisfying fits to the observed band profiles from higher rotational levels.

The effective temperature of the cold star can also be determined from photometric measurements. Munari et al. (2007) measured  $BVR_cI_c$  magnitudes of V838 Mon on 2005 Dec. 1, while Henden et al. (2006) measured  $UBVR_cI_c$  on 2005 Dec. 25 and  $JHK'$  magnitudes on Dec. 18. Thus the photometry was done  $\sim 2$  months after our spectroscopy. Given very slow evolution of the object at that epoch we can safely assume that the magnitudes did not change significantly between October and December 2005. Applying the same procedure to the above photometric results as that used in Tylenda (2005), i.e. fitting a standard supergiant photometric spectrum with  $E_{B-V} = 0.9$  and taking into account a contribution from a standard B3V star, we have obtained a spectral type of M6–7 and  $T_{\text{eff}} \simeq 2480$  K. Adopting  $R = 3.1$  and a distance of 8 kpc (as in Tylenda 2005) the effective radius and luminosity of V838 Mon are  $\sim 840 R_{\odot}$  and  $\sim 2.4 \times 10^4 L_{\odot}$ , respectively. The resultant fit is shown in Fig. 7. When fitting a blackbody to the  $IJK$  magnitudes, a temperature of 2320 K has been obtained and, correspondingly, an effective radius of  $\sim 905 R_{\odot}$  and a luminosity of  $\sim 2.2 \times 10^4 L_{\odot}$ . The blackbody fit (with the contribution from the B3V companion added) is shown as a dashed curve in Fig. 7. Thus the estimates of  $T_{\text{eff}}$  obtained from the photometric measurements are well consistent with the effective temperature we used to model the cold photosphere.

The photosphere model spectrum was then used as an underlying spectrum absorbed in the outflowing molecular gas. In radiative transfer modeling of absorption in the outflow (scattering was not included), the gas was treated as a plane-parallel homogeneous slab of matter.

<sup>9</sup> <ftp://ftp.hs.uni-hamburg.de/pub/outgoing/phoenix/NG-giant>



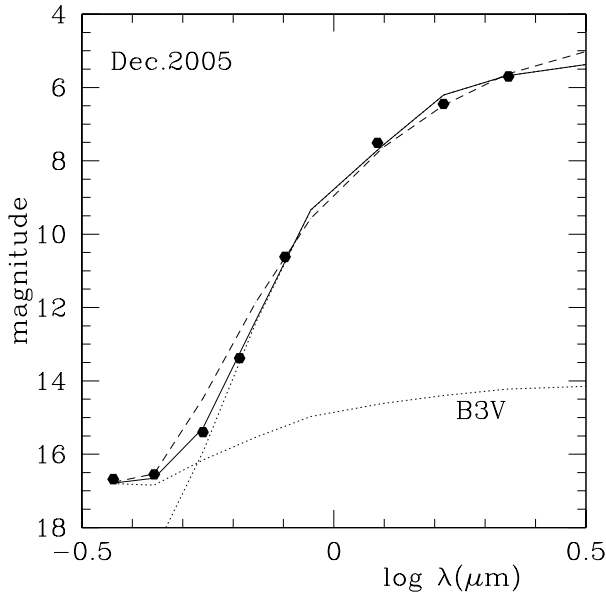


FIG. 7.— Model spectra fitted to the photometric ( $UBVR_cI_cJHK'$  – full points) measurements of V838 Mon in December 2005. Dotted curves – contributions from the supergiant and the B3V star. Full curve – final fit (sum of the dotted ones). Dashed curve – fit of a blackbody to the  $I_cJHK'$  measurements. See the text for more details.

In this one-dimensional approach three parameters characterize the outflowing gas, i.e. column density of an absorbing molecule, excitation temperature (the same for rotational and vibrational components), and a radial velocity of the slab (no velocity gradient was implemented). Finally, to the resultant spectrum a photospheric contribution of a B3V star was added (a synthetic spectrum of  $T_{\text{eff}} = 18000$  K and  $\log g = 4.0$  was used for this purpose – see Sect. 6).

It should be noted that the above approach was not meant to reproduce the observed spectrum in the whole spectral range. Simulations were performed separately for different narrow spectral regions and usually for one molecule at once. It allowed us to identify and study individual bands dominating in a given spectral range. With this modeling procedure rough estimates of physical parameters of the outflowing material (excitation temperature, column densities, radial velocity) were also possible in a number of cases.

A list of the identified molecular bands is presented in Table 3. The first column of the table gives observed wavelengths of features. In most cases this is the wavelength of a bandhead formed by the R branch, but in a few cases this corresponds to a local minimum of the absorption feature formed by Q or P branches; otherwise an empty space is left. Column (2) contains laboratory wavelengths of the features. Columns (3), (4), and (5) specify the molecule name, the electronic system with a vibrational band identification, and the branch designation, respectively. Column (6) gives a heliocentric velocity of the feature, if a clear bandhead is observed. References to appropriate molecular data and comments on individual features can be found in the last two columns. Most of the identified molecular features are also indicated on the spectrograms in Figs. 1–3.

The spectrum is dominated by strong TiO absorption

bands, which are present in all parts of the HIRES spectrum. Prominent are also bands of VO, AlO, ScO, and YO. In the following subsections, we describe in some detail the identified features for each of the molecules.

### 5.1. TiO

Much effort was devoted to understand electronic transitions of TiO in laboratory (Phillips 1973), in astronomical observations (Ram et al. 1999), as well as in theoretical computations (Schwenke 1998). In the identification procedure, we mainly consulted databases of line positions computed from laboratory measurements (Jørgensen 1994; Plez 1998; Schwenke 1998). These line lists also provide data for bands not measured in laboratory and in these cases discrepancies between different sources are often significant. The lack of accurate spectroscopic data disables a detailed analysis of some TiO bands, e.g. the  $\gamma'$  (3,0) band close to 5350 Å and higher overtones of  $\gamma'$  bands.

We have identified three electronic systems of TiO in the spectrum of V838 Mon, i.e.,  $\alpha$  ( $C^3\Delta - X^3\Delta$ ),  $\gamma$  ( $A^3\Phi - X^3\Delta$ ), and  $\gamma'$  ( $B^3\Pi - X^3\Delta$ ). The molecular bands of the  $\gamma$  and  $\gamma'$  systems have generally a characteristic triple structure formed by their main branches. In the case of the  $\alpha$  transitions, the separation of branches is so small that the three components overlap and the triple structure is not seen. Additionally, in some bands of the  $\gamma$  and  $\gamma'$  systems, relatively strong satellite branches are observed, e.g. the  $R_{31}$  branch of the  $\gamma'$  (1,0) band at 5827 Å. Finally, we have also identified forbidden transitions of TiO in the spectrum. The latter point is discussed in Sect. 5.6.

The observed features of TiO arise both in the stellar photosphere and in the outflow. Although the latter component dominates formation of the observed bands, it would be impossible to satisfactorily reproduce a number of the observed features without a contribution from the photosphere. Unfortunately, we have not been able to set valuable constraints on the effective temperature, since there are only a few regions in the spectrum, where the stellar component dominates. Performed simulations show, however, that the selected atmospheric model with  $T_{\text{eff}} = 2400$  K works good in reproducing high excitation features seen in the spectrum (see below).

Nonetheless, the most prominent absorptions of TiO seen in the spectrum of V838 Mon arise in a low excitation environment. A comparison between the observations and spectra computed from our slab model with different excitation temperatures suggests a mean value of  $T_{\text{ex}} = 500 \pm 100$  K. Adopting this temperature and comparing the observed spectrum to the simulations of the  $\gamma'$  (2,0), (1,0), (0,0), and  $\gamma$  (2,0) bands, an estimate of the TiO column density of  $\sim 16.8$  dex  $\text{cm}^{-2}$  has been obtained. Assuming that all Ti is locked in TiO and taking a Ti atomic abundance of  $10^{-7}$  relative to hydrogen, a column density of hydrogen of  $\sim 23.8$  dex  $\text{cm}^{-2}$  has been derived.

A characteristic feature of the observed TiO spectrum is a strong saturation of bands originating from the ground vibrational state. The effect is clearly seen in the  $\gamma'$  (0,0) and (1,0) bands. In the  $\gamma'$  (2,0) band the saturation is weaker and completely disappears in the (3,0) band. Similarly, a strong saturation is seen in the

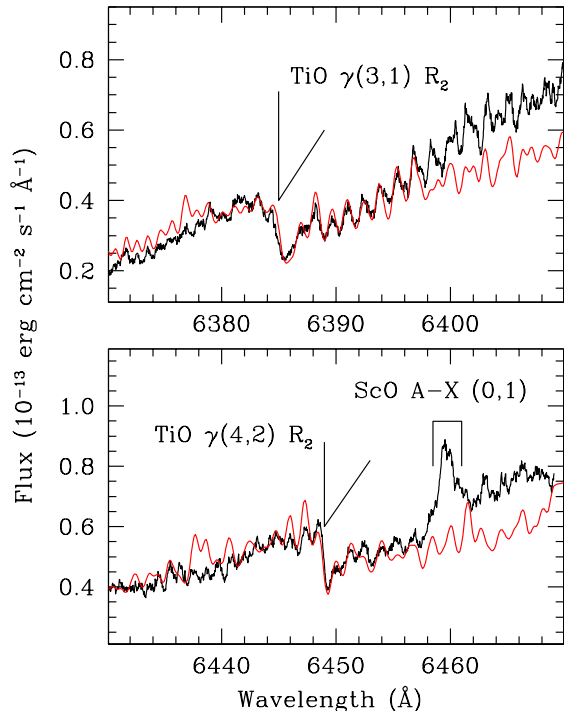


FIG. 8.— Rotational structure of highly excited levels of two  $\gamma$  bands of TiO. The observed spectrum (black line) is compared with simulations (red line). In order to fit the simulated rotational features to those in the observed spectrum, the simulated spectra have been shifted to a velocity of  $V_h = 58 \text{ km s}^{-1}$  and smoothed with a Gaussian with  $\text{FWHM} = 34 \text{ km s}^{-1}$ . An emission feature of ScO can easily be seen in the bottom panel (ScO was not included in the simulations shown here).

$\alpha$  (0,0), (1,0), (2,0) bands, and probably also in the (3,0) and (4,0) bands. In the red part of the analyzed spectrum, the  $\gamma$  (0,0) and (1,0) bands are saturated. Due to the strong saturation in the  $\gamma$  and  $\gamma'$  systems the triple structure of the bands can be seen only through weak emission-like features that appear between the saturated components, see e.g. the  $\gamma$  (0,0) and (1,0) bands at  $6670 \text{ \AA}$  and  $7100 \text{ \AA}$  (Fig. 3).

Radial velocities of some TiO bands can be determined by comparing rotational features of the observed bands with simulated spectra. Although the rotational structure is completely smoothed in the observed bandheads, it is recognizable in those parts of the spectrum, where only absorptions from higher rotational levels are present. Two examples of such rotational features are shown in Fig. 8, where a simulated spectrum is overplotted on the observed one. The cold slab had an excitation temperature of  $500 \text{ K}$  in the simulations. Note however that the contribution from the slab is negligible in the  $\gamma(3,1)$  and (4,2) bands. To fit the rotational components the modelled spectrum has been shifted to  $V_h = 58 \pm 5 \text{ km s}^{-1}$ . Since these rotational features coming from high excitation levels are predominantly formed in the atmosphere of the central star, the derived velocity is expected to be close to the radial velocity of the star.

Radial velocities can also be determined from the observed positions of bandheads. In the case of the TiO bands present in our spectrum formation of a bandhead

is often strongly influenced by presence of satellite bands and a non-negligible isotopic shift in wavelength. An example is presented in panel (a) of Fig. 9. This head, belonging to the  $\alpha$  (2,0) band, is formed by the  $R_2$  branch and a contribution from satellite bands is small in this case. However, as can be seen in the rotational profile<sup>10</sup> overplotted on the spectrum in Fig. 9, the head is actually formed by multiple components. The strongest ones belong to the three main TiO isotopomers, i.e.,  $^{46}\text{Ti}^{16}\text{O}$ ,  $^{47}\text{Ti}^{16}\text{O}$ , and  $^{48}\text{Ti}^{16}\text{O}$ . For solar Ti isotopic ratios, i.e. 9.3,10.1,13.4,13.8 for 48/46,48/47,48/49,48/50, respectively (Cowley 1995), all the isotopic components should significantly contribute to the shape of the  $\alpha$  (2,0) bandhead. Since they are not distinguishable in the observed smooth head, only a position of the most blueshifted component belonging to the  $^{46}\text{Ti}$  isotopomer can be measured with a reasonable accuracy. In this way a velocity of  $V_h = -67 \text{ km s}^{-1}$  has been inferred.

Another example of a TiO complex bandhead is shown in panel (b) of Fig. 9. As seen in the rotational profile, the structure of the  $\gamma'$  (1,0) bandhead is even more elaborate than in the previous example. This is due to the presence of multiple heads formed by satellite branches. The observed head is again very smooth and individual components, clearly distinguishable in the overplotted rotational profile, are not seen in the observed spectrum. An estimate of the outflow velocity is very uncertain in this case, but by fitting the rotational profile to the overall absorption profile of the band, a velocity of  $V_h = -58 \pm 10 \text{ km s}^{-1}$  has been derived.

As can be found in Table 3, the most blueshifted molecular component is observed in the  $\alpha$  (0,0) band at  $5164.6 \text{ \AA}$ . A velocity of  $-125 \text{ km s}^{-1}$  has been derived assuming that the blue edge of the head is formed by the  $^{46}\text{TiO}$  isotopomer, instead of the most abundant  $^{48}\text{TiO}$ . A similar velocity was found for the  $\alpha$  (1,0) band at  $4952.6 \text{ \AA}$ .

The derived radial velocities of TiO features are in a range between  $58 \text{ km s}^{-1}$  and  $-125 \text{ km s}^{-1}$ . It is reasonable to assume that the molecular absorption arises in an outflow with a velocity gradient. This can explain different velocities of the bands with different excitation requirements, and can also account for the observed smooth structure of the bandheads.

## 5.2. AlO

We based our identification procedure of the AlO bands on an analysis of the  $B^2\Sigma^+ - X^2\Sigma^+$  system performed in Coxon & Naxakis (1985). Absolute strengths of the electronic transitions were taken from Partridge et al. (1983).

The blue-green ( $B^2\Sigma^+ - X^2\Sigma^+$ ) band system of AlO is evidently present in the analyzed spectrum. The most prominent feature is the saturated (0,0) band with a main head at  $4842 \text{ \AA}$ , see panel (c) in Fig. 9. Three bandheads of different branches are close enough to form this relatively sharp head. In this case a radial velocity can be measured accurately and we have found  $V_h = -82 \pm 6 \text{ km s}^{-1}$ .

<sup>10</sup> A rotational profile means here a computed and smoothed profile of normalized absorption features of a band and it should not be confused with a full simulation from our model involving stellar photosphere and an absorbing cool slab as described in Sect. 5.

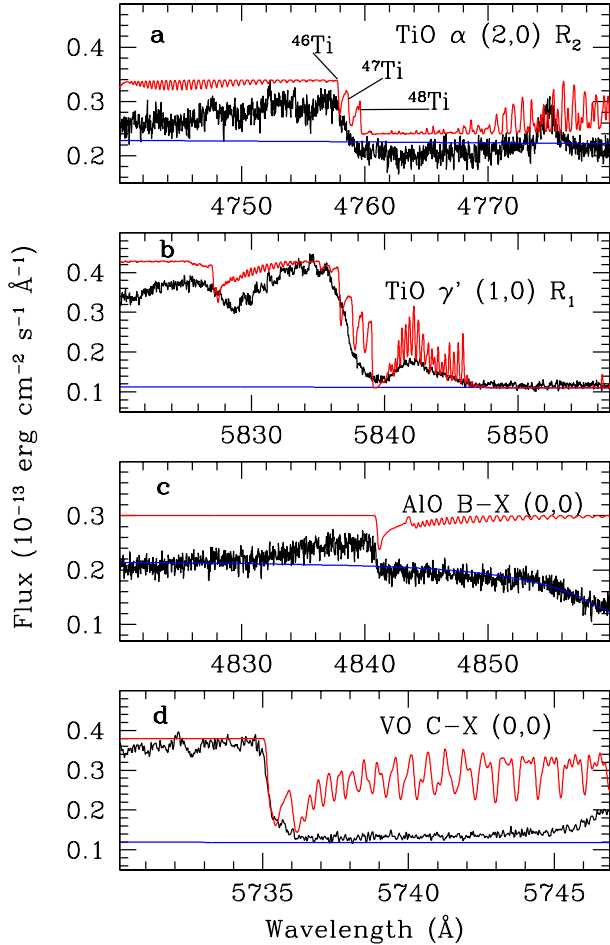


FIG. 9.— Examples of observed (black line) bandheads of TiO, AIO, and VO, together with their simulated rotational profiles (red). On each panel a synthetic spectrum of a B3V star is also shown (blue). The rotational profiles were shifted in velocity to fit the observed bandheads. (a) The  $\alpha$  (2,0) bandhead of TiO. The three heads clearly distinct in the simulated profile correspond to  $^{46}\text{TiO}$ ,  $^{47}\text{TiO}$ , and  $^{48}\text{TiO}$  isotopomers. The profile was shifted in velocity by  $-67\text{ km s}^{-1}$ . (b) The  $\gamma'$  (1,0) bandhead of TiO. This head is formed by multiple strong satellite branches and defining a reference laboratory position of the blue edge of the absorption feature is problematic. (c) The sharp B-X (1,0) bandhead of AIO. In this case the reference laboratory position is well defined. The velocity shift is  $-82\text{ km s}^{-1}$ . (d) The C-X (0,0) bandhead of VO. As seen in the computed profile, this head has a double structure when the band is not very saturated. The velocity shift is  $-78\text{ km s}^{-1}$ .

Higher vibrational overtones,  $\Delta v = +1$  and  $\Delta v = +2$ , of the B-X system can also be recognized in the spectrum of V838 Mon. The more intense  $\Delta v = +1$  overtone is seen up to the (6,5) band around  $4754\text{ \AA}$ . The radial velocity of the bandheads of the first overtone cannot be defined accurately due to the poor quality of the spectrum in the blue range. However, the wavelengths of bands from higher vibrational levels imply a velocity of  $V_h \simeq 58\text{ km s}^{-1}$ . The  $\Delta v = +2$  overtone is only hardly seen in the spectrum. The most intense (2,0) band is contaminated by the He I  $4471\text{ \AA}$  line of the B3V star.

In the green part of the spectrum, vibrational bands belonging to the  $\Delta v = -1$  sequence are clearly visible.

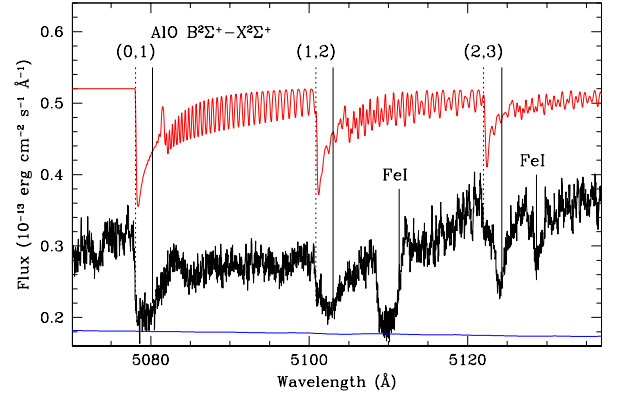


FIG. 10.— Observed spectrum (black line) of the A-X  $\Delta v = -1$  subtone of AIO together with its rotational profile computed for an excitation temperature of  $1500\text{ K}$  (red). The profile was shifted in velocity by  $-82\text{ km s}^{-1}$ . The dotted lines mark positions of the bandheads if shifted to  $V_h = -82\text{ km s}^{-1}$ , while the solid vertical lines are drawn for  $V_h = 58\text{ km s}^{-1}$ . The blue line marks the flux level of the B3V companion.

The bands are shown in Fig. 10. The (0,1) band at  $5079\text{ \AA}$  is particularly strong. Its bandhead is saturated and shifted to  $V_h = -82\text{ km s}^{-1}$ . One can also distinguish other members of the same overtone originating from higher vibrational levels up to  $v'' = 4$ . According to our simulations, these bands, to be observed, require a rather high excitation temperature of about  $1500\text{ K}$ , which suggests that they originate in, or close to, the atmosphere of the star. However, sharp bandheads belonging to transitions with  $v'' \leq 3$  are shifted to a velocity  $V_h = -82\text{ km s}^{-1}$ , which is inconsistent with the stellar velocity. The velocity rather indicates that the absorbing gas is located in outer parts of the outflow. Note that this velocity is almost the same as that of the narrow absorbing component seen in several atomic lines, e.g. Rb I (see Sect. 4.2).

### 5.3. VO

The spectrum of V838 Mon shows strong vibrational bands of the  $\text{C}^4\Sigma^- - \text{X}^4\Sigma^-$  and  $\text{B}^4\Pi - \text{X}^4\Sigma^-$  systems of VO. For the purpose of our simulations a line list for these systems was computed using spectroscopic constants from Cheung et al. (1982). Rotational strength factors were taken from Kovács (1969) with corrections applied after Whiting et al. (1973). In the case of the B-X (0,0), (1,0), and (2,0) bands, a list of energy levels was generated by diagonalization of the perturbed Hamiltonian from Adam et al. (1995) and Cheung et al. (1994). The transformation matrices were next used to compute rotational strengths of individual lines to properly include effects of perturbations. The rotational structure of the (2,0) band was not analyzed in laboratory. Therefore spectroscopic parameters for this band were extrapolated from the lower overtones. Electronic strengths were taken from Karlsson (1997). Franck-Condon factors were computed with the LeRoy's codes<sup>11</sup> (Le Roy 2004, 2007).

As can be seen in panel (d) of Fig. 9, the unsaturated C-X (0,0) band has two heads. One is formed by the  $\text{R}_1$  and  $\text{R}_4$  branches, while the other, redshifted by  $1\text{ \AA}$ , is

<sup>11</sup> <http://leroy.uwaterloo.ca/programs/>

formed by  $R_2$  and  $R_3$ . Both are present in the observed spectrum and the former one appears at a velocity of  $-77 \text{ km s}^{-1}$ . A regular ladder of rotational lines of the (0,0) band formed by main P branches can be recognized starting at  $5753 \text{ \AA}$  (see Fig. 2). Fortunately, precise laboratory wavelengths are available for these lines and a detailed modeling of the band was possible. The simulations suggest that this part of the spectrum is formed at a low excitation temperature of  $\sim 300 \text{ K}$ . The derived velocity of the absorbing gas in the rotational transitions of the (0,0) band is  $V_h = 43 \text{ km s}^{-1}$ . From the heads of higher transitions of the C-X system, namely the (1,0) and (2,0) bands, velocities of  $-77 \text{ km s}^{-1}$  and  $-45 \text{ km s}^{-1}$  were derived, respectively.

Additionally, within the B-X system, the bands (0,0), (1,0), and (2,0) were identified. The (0,0) and (1,0) bands, together with their simulated spectra, are presented in Fig. 11. Most of the features of these bands are only slightly shifted from their laboratory wavelengths and the measured velocity is  $V_h = -2 \text{ km s}^{-1}$ . A rather uncertain value of  $\sim 350 \text{ K}$  was deduced from the simulations as an excitation temperature of the absorbing gas (mainly from the intensities of absorption features at  $7910 \text{ \AA}$  and  $7920 \text{ \AA}$ ). Furthermore, in order to reproduce some features seen in the spectra of the bands with higher vibrational numbers, e.g. the absorption feature at  $7474 \text{ \AA}$  belonging to the (2,1) band, it was necessary to add an additional layer of absorbing VO gas with a rather high excitation temperature, namely  $T_{\text{ex}} = 1500 \text{ K}$ . This hotter component, treated in the simulations as a slab between the stellar photosphere and the cold slab, appears at a velocity of  $\sim 58 \text{ km s}^{-1}$ .

Our simulations of the C-X (0,0), B-X (0,0) and (1,0) bands give satisfactory fits to the observations when a column density of the VO absorber is of  $\sim 16.4 \text{ dex cm}^{-2}$ . If we assume that all V is locked in VO molecules and taking the solar abundance of V relative to H of  $10^{-8}$ , this corresponds to a column density of H of  $\sim 24.4 \text{ dex cm}^{-2}$ . The result is consistent with a similar estimate performed from the TiO bands in Sect. 5.1.

#### 5.4. ScO

The only electronic system of ScO present in the spectrum is the  $A^2\Pi - X^2\Sigma^+$  system. Absorption features of the (0,0), (1,1), (2,1) bands are clearly seen in the green part of the spectrum. Moreover, one band of ScO, i.e. the (0,1) band, was found in emission. For the purpose of our simulations, line positions of the A-X (0,0) band were computed from the Hamiltonian diagonalization parameterized by Stringat et al. (1972) and Adams et al. (1968). Higher vibrational levels were approximated from data in NIST<sup>12</sup>. For the positions of transitions of the (1,0) band, Rice & Field (1986) was consulted. Strengths of rotational lines were found in the approach proposed in Herbig (1974). It should be noted, that although the line positions of the (0,0) band are exact, their strengths are only approximate.

Figure 12 shows a region of the observed spectrum covering two subbands of the (0,0) band. Simulations of this spectral region suggest the presence of at least two different velocity components. The bandhead formed by the

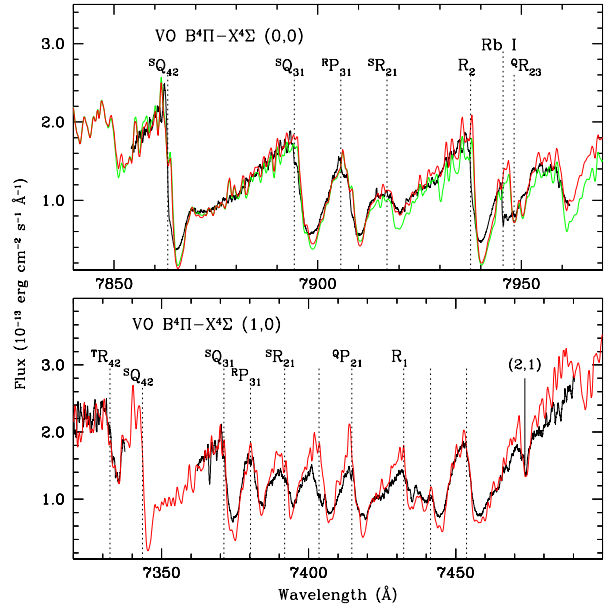


FIG. 11.— Comparison between the observed (black line) and simulated spectra of the B-X bands of VO. **Top:** the (0,0) band was simulated with the excitation temperatures of 350 K (red line) and 500 K (green line). The simulated spectra were shifted to a velocity of  $-2 \text{ km s}^{-1}$  and smoothed with a Gaussian with  $\text{FWHM} = 65 \text{ km s}^{-1}$ . The vertical lines mark positions of the bandheads for a radial velocity of  $-80 \text{ km s}^{-1}$ , which fits to the observed bandheads of  $^S Q_{42}$  and  $R_2$ , and to the blue edge of the Rb I profile. **Bottom:** the simulation of the (1,0) band obtained with two layers of the absorbing molecular gas with different temperatures, i.e. 500 K and 1500 K. The colder layer was shifted in velocity to  $-2 \text{ km s}^{-1}$ , while the warmer one, treated in our radiative transfer modeling as a layer between the stellar atmosphere and the cold slab, was shifted to a velocity of  $58 \text{ km s}^{-1}$ . The dotted lines mark positions of the bandheads for a radial velocity of  $-60 \text{ km s}^{-1}$ , which fits to the  $^T R_{42}$  and  $^S Q_{31}$  bandheads. The absorption feature at  $7474 \text{ \AA}$  belongs to the (2,1) band.

$^2\Pi_{3/2} \text{ } ^R Q_{2G} + ^R R_{2G}$  (at  $6036 \text{ \AA}$ ) and  $^2\Pi_{1/2} \text{ } ^Q Q_{1G} + ^Q R_{1G}$  (at  $6079 \text{ \AA}$ ) branches are shifted to  $-55 \text{ km s}^{-1}$  (as measured for the lowest part of the profile). The second velocity component at  $45 \text{ km s}^{-1}$  was found from the position of the head formed by the  $^2\Pi_{1/2} \text{ } ^R R_{1G}$  branch at  $6064.17 \text{ \AA}$ . This latter head is formed at a rather high rotational number, i.e.,  $N=58$ , contrary to the heads observed at  $-55 \text{ km s}^{-1}$ , which are formed at  $N=28$  and  $N=17$ . The relative velocity shift can be understood as a result of decreasing population of high rotational levels with increasing velocity in the observed outflow. A lack of accurate laboratory wavelengths disables an analysis of other absorption bands of ScO.

Remarkable is the presence of the A-X (0,1)  $^2\Pi_{3/2} \text{ } ^R Q_{2G}$  and  $^2\Pi_{1/2} \text{ } ^Q Q_{1G}$  subbands of ScO in emission at  $6408 \text{ \AA}$  and  $6458 \text{ \AA}$ , respectively (see bottom panel of Fig. 8 for the latter subband). The observed velocity of this features agrees well with the velocity of emission components seen in the atomic P-Cyg profiles (see Sect. 4.2). The origin of this molecular emission can be explained by fluorescent pumping of the upper electronic level by absorption in the (0,0)  $6090 \text{ \AA}$  and  $6132 \text{ \AA}$  subbands, clearly seen in the spectrum of V838 Mon.

<sup>12</sup> <http://physics.nist.gov/PhysRefDat/ASD/>



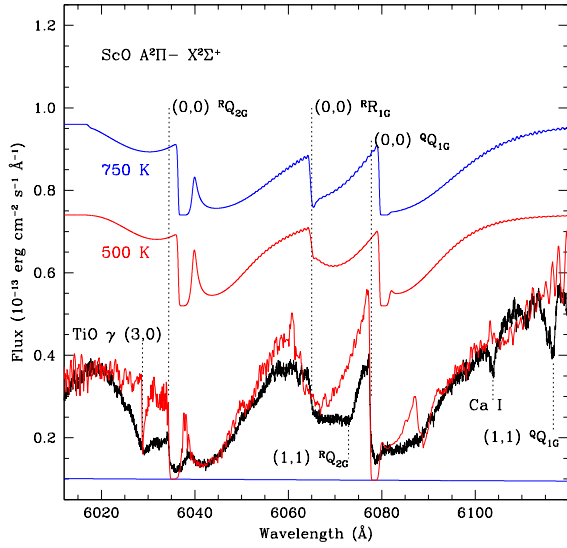


FIG. 12.— Comparison between the observed and simulated spectrum of the A–X (1,0) band of ScO. The two upper plots are rotational profiles of the band, computed for excitation temperatures of 750 K and 500 K (blue and red, respectively). They are shifted to a velocity of  $58 \text{ km s}^{-1}$ . The observed spectrum is drawn with a black line. Overlaid on it in red is a simulated spectrum with a molecular slab absorbing the light of the cool star as described in Sect. 5. The absorbing layer has an excitation temperature of 500 K and is shifted in velocity by  $-55 \text{ km s}^{-1}$ . The simulated spectrum is smoothed with a Gaussian with  $\text{FWHM} = 32 \text{ km s}^{-1}$ . The flux level of the B3V star is indicated with the blue line.

### 5.5. YO

All the features of YO identified in the spectrum of V838 Mon belong to the  $A^2\Pi-X^2\Sigma^+$  system. A list of the transitions used in our identification procedure was prepared on the basis of data provided in Bernard & Gravina (1983). There is another well known system of YO, i.e.  $B^2\Pi-X^2\Sigma^+$  around  $4819 \text{ \AA}$  (Bernard et al. 1979), but it falls into a spectral region of saturated TiO bands and was not found in our spectrum.

We performed a detailed simulation of the  $A^2\Pi_{3/2}-X^2\Sigma^+$  transition. The results of this simulations are shown in Fig. 13. The upper two plots in Fig. 13 are rotational profiles of the transition obtained for two excitation temperatures, 750 K and 500 K. It can be seen that a sharp edge of the (0,0) bandhead at  $5973 \text{ \AA}$  is formed with the higher temperature. In the observed spectrum this head is very smooth and resembles more the feature seen in the profile for 500 K, and this is a value we took for further simulations. It should be noted, however, that the observed profile of the band can be influenced by the physical structure of the wind, which is ignored in our simulations; in particular, a velocity gradient in the molecular outflow can smooth the shape of the bandheads, and even if the temperature is high, no sharp head would be observed. Nonetheless, to perform full simulations of the  $A^2\Pi_{3/2}-X^2\Sigma^+$  transition of YO it was necessary to include the  $\gamma(3,0)$  band of TiO as an additional important absorber in this spectral range. The green line in Fig. 13 shows the TiO contribution to the observed spectrum. The final simulation which

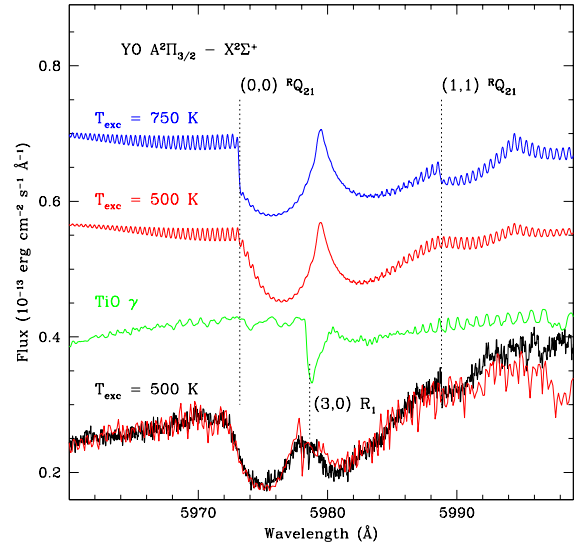


FIG. 13.— Same as in Fig. 12 but for the fine components of the electronic transitions of the  $A^2\Pi_{3/2}-X^2\Sigma^+$  feature of YO. The final simulation (bottom) includes an extra absorption of TiO, which is shown with a green line. The simulation was performed with a slab of 500 K and the stellar photosphere. All the computed spectra were shifted to a velocity of  $58 \text{ km s}^{-1}$  and smoothed with a Gaussian with  $\text{FWHM} = 37 \text{ km s}^{-1}$ .

includes absorption of YO and TiO with an excitation temperature of 500 K is shown at the bottom of Fig. 13. From the overall fit of the (0,0) band to the full simulation a velocity of  $V_h = -8 \text{ km s}^{-1}$  has been derived.

Note however that a sharp (1,1) bandhead formed by the  $RQ_{21}$  branch at  $5988 \text{ \AA}$  appears at higher excitation temperatures, at least 750 K, as can be seen from Fig. 13. Such a sharp feature seems to be present in the observed spectrum, suggesting that this absorption feature is formed in gas with a somewhat higher temperature than the one found for the (0,0) bandhead. This is confirmed by the measured velocity of the (1,1) bandhead,  $V_h = 58 \text{ km s}^{-1}$ , which is the same as that of other high-excitation features found in the spectrum.

### 5.6. TiO – forbidden transitions

Very interesting from the spectroscopical point of view is the presence of forbidden transitions of TiO, i.e. the  $c^1\Phi-X^3\Delta(0,0)$  band around  $4737 \text{ \AA}$  and the  $b^1\Pi-X^3\Delta(0,0)$  band at  $6832 \text{ \AA}$ . The stronger b–X band is shown in detail in Fig. 14. The intensities of the bands were predicted in *ab initio* calculations of ro-vibrational energy levels of the 13 lowest electronic states of TiO by Schwenke (1998). As shown in Fig. 14, our simulation can reproduce the forbidden bands quite well. The best fit indicates a velocity of  $V_h = -80 \text{ km s}^{-1}$  and an excitation temperature of about 500 K. However, when the column density found for other TiO bands (see Sect. 5.1) is assumed, oscillator strengths of the  $b^1\Pi-X^3\Delta$  band must be enhanced by a factor of  $70 \pm 35$  in order to reproduce the observations. To our knowledge this is the first, in astrophysics as well as in laboratory, observation of TiO forbidden bands.

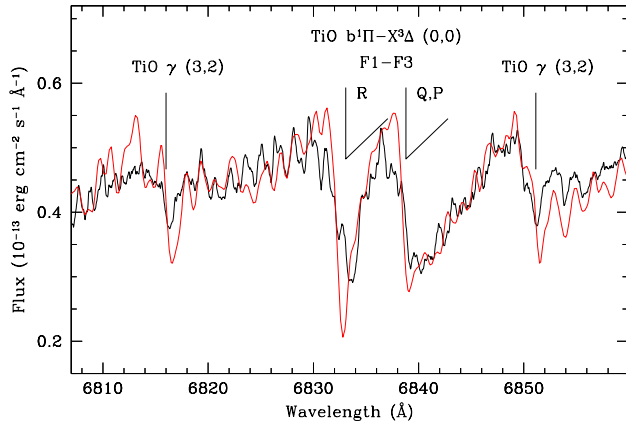


FIG. 14.— Observed and simulated spectrum of the forbidden band  $b^1\Pi-X^3\Delta (0,0)$  of TiO. The simulation (red line) was obtained with an excitation temperature of 500 K. It was shifted to a velocity  $V_h = -82 \text{ km s}^{-1}$  and smoothed with a Gaussian with  $FWHM = 32 \text{ km s}^{-1}$ .

## 6. PHOTOSPHERIC SPECTRUM OF THE B3V COMPANION

A number of broad absorption lines of the Balmer series, from  $H\beta$  down to at least  $H_{12}$ , as well as a few He I lines, can clearly be seen in the blue part of our spectrum (Fig. 1). These features are attributed to the B3V companion. We compared the observed spectrum to a grid of synthetic spectra *BSTAR2006*, generated with the *Synspec* program (Lanz & Hubeny 2007). Solar metallicity models, with effective temperatures between 15 000 and 30 000 K and gravities in the range  $\log g = 2.0 - 4.75$  were considered. A turbulent velocity of  $2 \text{ km s}^{-1}$  was adopted. Good fits to the observed spectrum were obtained for  $T_{\text{eff}} = 18\,000 \pm 2\,000 \text{ K}$  and  $\log g = 4 \pm 0.75$ . The low signal-to-noise ratio in the part dominated by the B3V star and uncertainties in the flux calibration did not allow us to obtain more precise estimates of the star parameters. In any case, the above values agree well with those expected for a B3V star. In the following discussion we use the synthetic spectrum with  $T_{\text{eff}} = 18\,000 \text{ K}$  and  $\log g = 4.0$ . This spectrum, broadened with a rotational velocity of  $250 \text{ km s}^{-1}$  (see below) and shifted to a radial velocity found for the hot star (see below), is overplotted on the observed spectrogram of V838 Mon in Figs. 1–3.

A comparison of the observed spectrum to the synthetic one shows that the absorption lines of the B3V companion are rotationally broadened. In order to find the rotational velocity, we convolved the synthetic profiles with a Gaussian profile broadened with a grid of rotational velocities (we made use of the *rotin3* program<sup>13</sup>). Note that this procedure does not take into account limb darkening nor gravitational darkening, which can be important for profile formation in a rapidly rotating star. Lines usually used to investigate rotational broadening of B-type stars, i.e. He I 4471 Å and Mg II 4481 Å, are weak, noisy, and affected by emission lines and/or molecular bands in our spectrum. However, we have found that in the green part of the spectrum the He I 5876 Å line

is relatively strong and has a “clean” profile. This green spectral region is dominated by the cool photosphere but, fortunately, in the spectral vicinity of the  $\lambda 5876$  line the flux from this component is practically reduced to zero due to a saturated TiO band (see Fig. 2) and the line from the B3V component is well seen. Thus, when determining the rotational velocity of the B3V component we relied mainly (but not only) on the profile of He I 5876 Å. Using the  $T_{\text{eff}}=18\,000 \text{ K}$ ,  $\log g=4.0$  template we found a projected rotational velocity  $V \sin i = 250 \pm 50 \text{ km s}^{-1}$ . This is a rather large value<sup>14</sup> and indicates that the rotation axis is close to the plane of the sky.

We also attempted to measure the radial velocity of the hot star. We used the Fourier cross-correlation method (Tonry & Davis 1979) as it is implemented in the IRAF’s task *rvcor*. As a template, we used our synthetic spectrum broadened to the rotation velocity of  $250 \text{ km s}^{-1}$ . The cross-correlation was performed for the region between 3815 Å and 4180 Å, with all emissions and ISM absorptions in this range removed manually. (We performed tests with ranges including  $H\beta$  and  $H\gamma$ , but they did not give reliable results. These spectral regions are too strongly contaminated by atomic emissions and molecular absorptions. Also, including the very noisy shortward part of the spectrum spoils the cross-correlation function and gives unrealistic results.) As a result we obtained a heliocentric velocity of  $37.0 \pm 16.8 \text{ km s}^{-1}$  [with a Tonry & Davis’ (1979)  $r$  value of 18.0], or correspondingly  $19.6 \pm 16.8 \text{ km s}^{-1}$  in to the local standard of rest. The error value was taken directly from the output of the *rvcor* procedure and, in our opinion, it is slightly overestimated.

## 7. INTERSTELLAR FEATURES

Several interstellar absorption features can be identified in our spectrum. The strongest ones are those of Ca II H, K and Na I D<sub>1</sub>, D<sub>2</sub>. They are shown in Fig. 15. Interstellar components can also be found in the deep P-Cyg absorption of K I at 7699 Å (see upper panel in Fig. 6). The Na I and K I interstellar absorptions in the spectrum of V838 Mon have already been studied in a number of papers (e.g. Kipper et al. 2004; Munari et al. 2005). As can be seen from Fig. 15, the profiles of the Ca II lines, not described in the literature so far, have a similar structure to those of Na I. All the four profiles displayed in Fig. 15 show three components at 32, 42, and 65  $\text{km s}^{-1}$ , similarly as observed in Munari et al. (2005). We note, however, that unlike previous studies, where the interstellar lines were observed in the spectrum of V838 Mon itself, the features presented in Fig. 15 are observed in the spectrum of the B3V companion. As can be seen from Figs. 1 and 2 the local continuum near the discussed lines comes from the B3V companion. At the wavelengths of the Ca II lines V838 Mon is too cool to emit any significant radiation, while at the wavelengths of the Na I lines an absorption band of TiO is so strong that it eats up practically all the flux from the cool supergiant. The fact that the interstellar line profiles in the spectrum of the B3V companion are very similar to

<sup>14</sup> For instance, in Abt et al. (2002) one finds that the mean projected rotational velocity for 106 dwarfs with spectral types B3–B5 is  $108 \pm 8 \text{ km s}^{-1}$ , and only 2.4% of the stars have  $V \sin i \geq 300 \text{ km s}^{-1}$ .

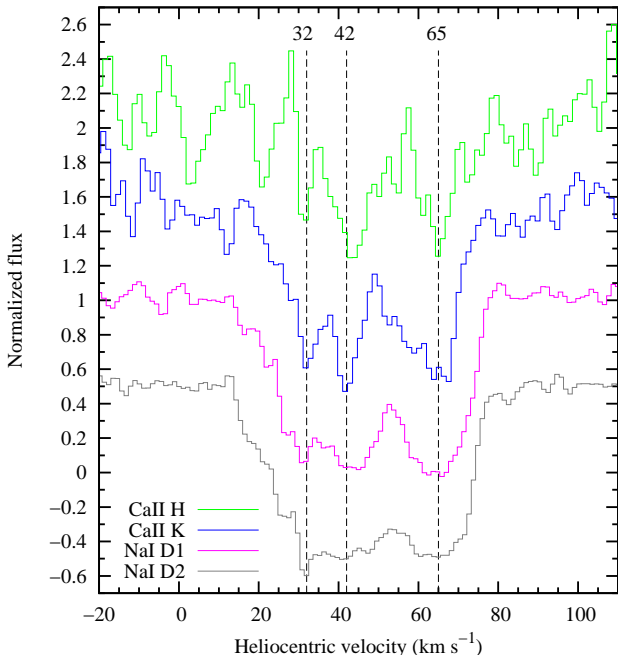


FIG. 15.— Interstellar doublets of Ca II and Na I. The curves, except Na I D<sub>1</sub>, are shifted in the vertical scale to better show the profile structures. The Ca II H profile is noisy as the line is observed near the core of the H $\epsilon$  absorption, where the stellar flux is very low (see Fig. 1). Three main absorption components at 32, 42, and 65 km s<sup>-1</sup> are marked with dashed vertical lines.

those in the spectrum of V838 Mon itself is consistent with the idea that both stars are related, at least that they are at a similar distance.

We have identified six diffuse interstellar bands (DIBs) in our spectrum, i.e., at  $\lambda\lambda 4428, 5780, 5797, 6284, 6614,$  and  $7224$  [the central wavelengths are taken from Herbig (1995)]. They all are redshifted to a heliocentric velocity of  $\sim 60$  km s<sup>-1</sup>. It is well known that equivalent widths of the features at 5780 and 5797 Å correlate very well with interstellar extinction. Using conversion formulae from Herbig (1975) we derived  $E_{B-V}$  of 0.95 and 0.90 for the DIBs at 5780 Å and 5797 Å, respectively. Taking the relation from Herbig (1993), which is based on a larger number of data points, gives  $E_{B-V} \simeq 1.00$  for both features. Given considerable uncertainty of these estimates, due to uncertainties in the equivalent width measurements and the intrinsic scatter in the relations used, our result is consistent with  $E_{B-V} \simeq 0.9$  obtained in other studies [as summarized in Tylenda (2005)].

## 8. SUMMARY

We have obtained a spectrum of V838 Mon on 2005 October 13 using the Keck/HIRES instrument. The spectrum of a resolving power of  $\sim 34000$  covered a wavelength range of  $3720 - 7960$  Å. The spectrum is very complex and shows numerous spectroscopic features which can be identified as arising from different components or environments. V838 Mon itself, i.e. the object which erupted in 2002, is seen mainly in the green and red parts of the spectrum as a cool continuum with strong, broad and complex molecular absorptions. Numerous atomic lines showing P-Cyg profiles or broad absorption features are also present in this component. The blue part of the spectrum is dominated by a photospheric spectrum of

the B3V companion, showing broad absorptions lines of H I and He I. In the blue and green parts of the spectrum, numerous emission lines can be identified. These mostly arise from forbidden transitions in singly ionized iron. Finally, several absorption features of interstellar origin have been identified. These include atomic resonance lines as well as DIBs.

The numerous [Fe II] emission lines observed in our spectrum evidently arise from rarefied and (partly) ionized matter. All the lines show the same profile, which can be well fitted with a Lorentzian profile. The lines are centred at a heliocentric radial velocity of  $\sim 13$  km s<sup>-1</sup> and have a typical FWHM of  $\sim 80$  km s<sup>-1</sup>.

In the cores of the photospheric absorption lines of the B3V companion we see weak emission features. The double feature in the H $\beta$  line can be interpreted as a single emission with a narrow absorption superimposed on it. The derived parameters of the emission component are close to those of the [Fe II] lines. This suggests that the Balmer emission features arise from the same environment as the [Fe II] emission lines.

The spectrum displays a number of strong atomic, mostly resonance, lines with P-Cyg profiles. Evidently V838 Mon, being almost 4 years after its outburst, continues losing mass. The emission component typically peaks at a heliocentric velocity of  $\sim 80$  km s<sup>-1</sup>, while the absorption component usually extends from  $\sim 50$  km s<sup>-1</sup> to  $\sim -100$  km s<sup>-1</sup>. The absorption component often shows a complex profile. In particular, in a few lines a strong and narrow absorption component is clearly seen at a velocity of  $\sim -80$  km s<sup>-1</sup>. A few atomic lines were observed to show pure absorption profiles.

The spectrum from the cool component is dominated by numerous, often very strong, molecular bands in absorption. Some bands are so deep that the flux from the cool component practically goes to zero. In these cases we have a sort of spectral windows, through which we can see the B3V companion, even in the red part of the spectrum. All the identified bands are from oxides. They include TiO, VO, AlO, ScO, and YO.

Our analysis shows that the bands are formed in different regions. Some of them, especially those from highly excited states, are formed, at least partially, in the photospheric regions. The temperature in these layers is as high as  $\sim 2400$  K. These bands show a heliocentric radial velocity of  $\sim 58$  km s<sup>-1</sup>, which we identify as a radial velocity of V838 Mon itself.

Most of the bands are formed in regions significantly cooler than the photospheric ones. The vibrational temperatures derived from some bands go down to  $\sim 500$  K. These are usually very strong bands arising from ground states. The radial velocity of these bands is usually much lower than that of the photospheric regions and goes down to  $\sim -125$  km s<sup>-1</sup>. Overall, our analysis of the molecular bands shows that they are mostly formed in outflowing matter with a significant velocity gradient.

We have detected bands arising from forbidden transitions in TiO. As far as we know, these are first observations of TiO forbidden transitions in astrophysical objects.

The observed spectrum of the B-type companion, seen primarily in the blue part of our spectrum, can be fitted with a model atmosphere spectrum with solar abundances, effective temperature of  $\sim 18000$  K, and a grav-



ity,  $\log g \simeq 4.0$ . These values agree well with those expected for a B3V star. The absorption lines are significantly broadened, which we interpret as a rotational broadening with a velocity,  $V \sin i \simeq 250 \text{ km s}^{-1}$ . We have derived a heliocentric radial velocity of the B3V companion of  $37 \pm 17 \text{ km s}^{-1}$ .

Several interstellar absorption features are seen in our spectrum. They include lines of Ca II, Na I, and K I, as well as DIBs. The lines of Ca II and Na I are observed in the spectrum of the B3V companion. Their profiles are very similar to those observed in the spectrum of V838 Mon during the 2002 outburst. This result is consistent with the idea that V838 Mon and the B3V companion are related objects. From equivalent widths of diffuse interstellar bands we have estimated an interstellar reddening of  $E_{B-V} \simeq 0.9 - 1.0$ , which agrees well with interstellar extinction values obtained by other authors using other methods.

A detailed analysis and interpretation of the data presented in the present paper, as well as of data from other sources, will be done in a forthcoming paper.

MS, RT, and TK were supported by the Polish Ministry of Science and Higher Education under grant no. N203 004 32/0448, for which they are grateful. TK wishes to thank T. Tomov for his helpful advises on data reduction and spectrum analysis with IRAF. MK was supported by the Foundation for Polish Science through a FOCUS grant and fellowship, by the Polish Ministry of Science and Higher Education through grants N203 005 32/0449 and 1P03D 021 29. MG acknowledges support by Polish KBN grant no. 1P03d 017 27 and SALT International Network grant no. 76/E-60/SPB/MSN/P-03/DWM 35/2005-2007. This paper uses observations made at the South African Astronomical Observatory (SAAO).

The authors wish to recognize and acknowledge the very significant cultural role and reverence that the summit of Mauna Kea has always had within the indigenous Hawaiian community. We are most fortunate to have the opportunity to conduct observations from this mountain.

*Facilities:* Keck:I (HIRES), Radcliffe (Grating Spectrograph)

#### REFERENCES

- Abt, H. A., Levato, H., & Grosso, M. 2002, *ApJ*, 573, 359  
 Adam, A. G., Barnes, M., Berno, B., Bower, R. D., & Merer, A. J. 1995, *Journal of Molecular Spectroscopy*, 170, 94  
 Adams, A., Klemperer, W., & Dunn, T. M. 1968, *Canadian Journal of Physics*, 46, 2213  
 Barsukova, E., Goranskij, V., Abolmasov, P., & Fabrika, S. 2006, *ATel*, 803  
 Bernard, A., Bacis, R., & Luc, P. 1979, *ApJ*, 227, 338  
 Bernard, A., & Gravina, R. 1983, *ApJ*, 52, 443  
 Bond, H. E. 2006, *ATel*, 966  
 Chauville, J., Zorec, J., Ballereau, D. et al. 2001, *A&A*, 378, 861  
 Cheung, A. S.-C., Hajigeorgiou, P. G., Huang, G., Huang, S.-Z., & Merer, A. J. 1994, *Journal of Molecular Spectroscopy*, 163, 443  
 Cheung, A. S.-C., Hansen, R. C., & Merer, A. J. 1982, *Journal of Molecular Spectroscopy*, 91, 165  
 Cowley, C. R. 1995, *An Introduction to Cosmochemistry* (Cambridge: Cambridge Univ. Press)  
 Coxon, J. A., & Naxakis, S. 1985, *Journal of Molecular Spectroscopy*, 111, 102  
 Crause, L. A., Lawson, W. A., Kilkeny, D., et al. 2003, *MNRAS*, 341, 785  
 Goranskij, V. 2006, *ATel*, 964  
 Hauschildt, P. H., Allard, F., Ferguson, J., Baron, E., & Alexander, D. R. 1999, *ApJ*, 525, 871  
 Henden, A., Munari, U., & Navasardyan, H. 2006, *IAU Circ.* 8655  
 Herbig, G. H. 1974, *ApJ*, 188, 533  
 Herbig, G. H. 1975, *ApJ*, 196, 129  
 Herbig, G. H. 1993, *ApJ*, 407, 142  
 Herbig, G. H. 1995, *ARA&A*, 33, 19  
 Hocking, W. H., Gerry, M. C. L., & Merer, A. J. 1979, *Canadian Journal of Physics*, 57, 54  
 Iben, I. Jr., & Tutukov, A. V. 1992, *ApJ*, 389, 369  
 Jørgensen, U. G. 1994, *A&A*, 284, 179  
 Karlsson, L., Lindgren, B., Lundevall, C., & Sassenberg, U. 1997, *Journal of Molecular Spectroscopy*, 181, 274  
 Kimeswenger, S., Lederle, C., Schmeja, S., & Armsdorfer, B. 2002, *MNRAS*, 336, L43  
 Kipper, T., Klochkova, V. G., Annuk, K. et al. 2004, *A&A*, 416, 1107  
 Kipper, T., & Škoda, P. 2007, in *ASP Conf. Ser.* 363, *The Nature of V838 Mon and its Light Echo*, ed. R. L. M. Corradi & U. Munari (San Francisco: ASP), 231  
 Kopp, I., Lindgren, R., Rydh, B. 1974, *Table of Band Features of Diatomic Molecules in Wavelength Order* (Stockholm: Univ. Stockholm)
- Kovács, I. 1969, *Rotational Structure in the Spectra of Diatomic Molecules* (London: Adam Hilger Ltd.)  
 Lanz, T., & Hubeny, I. 2007, *ApJS*, 169, 83  
 Lawlor, T. M. 2005, *MNRAS*, 361, 695  
 Le Roy, R. J., 2004, *Univ. of Waterloo Chemical Physics Research Report CP-657R*, 2004  
 Le Roy, R. J., 2007, *Univ. of Waterloo Chemical Physics Research Report CP-663*, 2007  
 Massey, P. 1997, *A User's Guide to CCD Reductions with IRAF*, <http://iraf.net/irafdocs/>  
 Moore, C. E. 1945, *A Multiplet Table of Astrophysical Interest, Contributions from the Princeton University Observatory No.20* (Princeton: Princeton Univ. Obs.)  
 Munari, U., Corradi, R. L. M., Henden, A. et al. 2007, *A&A*, 474, 585  
 Munari, U., Desidera, S. & Henden, A. 2002a, *IAU Circ.*, 8005  
 Munari, U., Henden, A., Kiyota, S., et al. 2002b, *A&A*, 389, L51  
 Munari, U., Henden, A., Vallenari, A. et al. 2005, *A&A*, 434, 1107  
 Partridge, H., Langhoff, S. R., Lengsfeld III, B. H., & Liu, B. 1983, *J. Quant. Spectrosc. Rad. Transfer*, 30, 449  
 Phillips, J. G. 1973, *ApJS*, 26, 313  
 Plez, B. 1998, *A&A*, 337, 495  
 Ram, R. S., Bernath, P. F., Dulick, M., & Wallace, L. 1999, *ApJS*, 122, 331  
 Rice, S. F., & Field, R. W. 1986, *Journal of Molecular Spectroscopy*, 119, 331  
 Schwenke, D. W. 1998, *Chemistry and Physics of Molecules and Grains in Space. Faraday Discussions No. 109*, 321  
 Soker, N. & Tyndra, R. 2003, *ApJ*, 582, L105  
 Stringat, R., Athénour, C., & Femenas, J. L. 1972, *Can. J. Phys.* 50, 395  
 Suzuki, N., Tytler, D., Kirkman, D., O'Meara, J. M., & Lubin, D. 2003, *PASP*, 115, 1050  
 Tonry, J. & Davis, M. 1979, *AJ*, 84, 1511  
 Tyndra, R. 2005, *A&A*, 436, 1009  
 Tyndra, R. & Soker, N. 2006, *A&A*, 451, 223  
 van Dokkum, P.G. 2001, *PASP*, 113, 1420  
 Vogt, S.S., Allen, S. L., Bigelow, B. C. et al. 1994, *Proc. SPIE*, 2198, 362  
 Whiting, E. E., Paterson, J. A., Kovács, I., & Nicholls, R. W. 1973, *Journal of Molecular Spectroscopy*, 47, 84

TABLE 1  
 IDENTIFIED EMISSION LINES

$\lambda_{\text{lab}}^{\text{air}}$ (Å)	Ion	Multiplet	Flux	Notes
3883.820	[Fe II]?	24F	...	a
3993.059	[Ni II]?	4F	...	...
4101.734	H $\delta$	1	...	...
4177.196	[Fe II]	21F	3.355e-15	b
4201.172	[Ni II]?	3F	...	...
4243.969	[Fe II]	21F	5.028e-14	c,d
4244.813	[Fe II]	21F	1.448e-14	c,d
4276.829	[Fe II]	21F	5.469e-14	...
4287.394	[Fe II]	7F	1.423e-13	...
4305.890	[Fe II]	21F	1.292e-14	...
4319.619	[Fe II]	21F	2.852e-14	...
4326.237	[Ni II]?	3F	...	...
4340.464	H $\gamma$	1	...	...
4346.852	[Fe II]	21F	...	c
4352.778	[Fe II]	21F	2.448e-14	...
4358.360	[Fe II]	21F	2.842e-14	d
4359.333	[Fe II]	7F	1.022e-13	d
4372.427	[Fe II]	21F	2.940e-14	...
4382.742	[Fe II]	6F	...	...
4413.781	[Fe II]	7F	1.109e-13	c,d
4416.266	[Fe II]	6F	5.579e-14	c,d
4432.447	[Fe II]	6F	...	...
4452.098	[Fe II]	7F	3.221e-14	...
4457.945	[Fe II]	6F	2.627e-14	...
4474.904	[Fe II]	7F	1.817e-14	...
4488.749	[Fe II]	6F	8.752e-15	...
4492.634	[Fe II]	6F	4.873e-15	b
4509.602	[Fe II]	6F	7.680e-15	e
4514.900	[Fe II]	6F	6.475e-15	e
4639.667	[Fe II]	4F	1.049e-14	f
4664.440	[Fe II]	4F	3.666e-15	e
4728.068	[Fe II]	4F	2.069e-14	...
4774.718	[Fe II]	20F	1.120e-14	...
4814.534	[Fe II]	20F	4.495e-14	...
4861.325	H $\beta$	1	...	...
4874.485	[Fe II]	20F	1.459e-14	...
<i>inter-chip gap</i>				
4973.388	[Fe II]	20F	1.836e-14	g
5005.512	[Fe II]	20F	2.225e-14	...
5018.440	Fe II	42	2.570e-14	c,d
5020.233	[Fe II]	20F	1.163e-14	c,d
5041.024	Si II?	5	...	...
5043.519	[Fe II]	20F	...	...
5055.984	Si II?	5	...	c
5056.317	Si II?	5	...	c
5158.001	[Fe II]	18F	3.723e-14	c,d
5158.777	[Fe II]	19F	2.433e-14	c,d
5163.951	[Fe II]	35F	...	...
5169.033	Fe II	42	2.411e-14	...
5181.948	[Fe II]	18F	6.598e-15	...
5184.788	[Fe II]	19F	1.915e-15	b
5197.902	[N I]	1F	...	h
5220.059	[Fe II]	19F	1.203e-14	g
5261.621	[Fe II]	19F	2.979e-14	f
5268.874	[Fe II]	18F	...	...
5273.346	[Fe II]	18F	5.160e-14	f
5333.646	[Fe II]	19F	2.506e-14	f
5347.653	[Fe II]	18F	...	c
5376.452	[Fe II]	19F	2.388e-14	...
5477.241	[Fe II]	34F	8.680e-15	g
5527.609	[Fe II]	34F	1.677e-14	g
5577.339	[O I]	3F	...	...
5746.966	[Fe II]	34F	1.329e-14	...
6300.304	[O I]	1F	...	...
6363.776	[O I]	1F	...	...
<i>inter-chip gap</i>				
7155.160	[Fe II]	14F	3.861e-15	...

NOTE. — The integrated line fluxes were measured on dereddened spectra and they are given in units of  $\text{erg cm}^{-2} \text{s}^{-1}$ .

<sup>a</sup> multiplet 24 absent in NIST

<sup>b</sup> weak line; flux uncertain

<sup>c</sup> blend

<sup>d</sup> flux measurement obtained with a deblending procedure

<sup>e</sup> line with poorly defined profile; flux uncertain

TABLE 2  
 P-CYGN AND ABSORPTION LINES

$\lambda_{\text{lab}}^{\text{air}}$ (Å)	Ion	Multiplet	Profile type	Notes
3933.663	Ca II K	1	absorption	a
3968.468	Ca II H	1	absorption	a
4254.332	Cr I	1	absorption	b
4274.796	Cr I	1	absorption	b
4289.716	Cr I	1	absorption	b
4545.945	Cr I	10	absorption	...
4554.033	Ba II?	1	absorption	c
4571.096	Mg I	1	P-Cygni	d
4580.043	Cr I	10	absorption	...
4613.357	Cr I	21	absorption	...
4616.120	Cr I	21	absorption	...
4646.148	Cr I	21	absorption	e
4651.282	Cr I	21	absorption	e
<i>inter-chip gap</i>				
5060.078	Fe I	1	absorption	...
5110.413	Fe I	1	P-Cygni	f
5127.681	Fe I?	1	absorption	...
5147.479	Ti I	4	absorption	g
5152.185	Ti I	4	absorption	g
5204.506	Cr I	7	absorption	e
5206.038	Cr I	7	absorption	e
5208.419	Cr I	7	P-Cygni?	e
5247.049	Fe I?	1	absorption	...
5264.157	Cr I	18	absorption	e
5265.723	Cr I	18	absorption	e
5296.691	Cr I	18	absorption	e
5298.277	Cr I	18	P-Cygni	e
5300.744	Cr I	18	absorption	...
5345.801	Cr I	18	absorption	e
5348.312	Cr I	18	absorption	e
5394.676	Mn I	1	P-Cygni	...
5409.772	Cr I	18	P-Cygni	...
5426.237	Ti I	3	absorption	g?
5432.546	Mn I	1	P-Cygni	...
5535.481	Ba I	2	P-Cygni	...
5698.520	V I	35	absorption	...
5703.580	V I	35	absorption	...
5706.980	V I	35	absorption	...
5727.050	V I	35	absorption	e
5727.650	V I	35	absorption	e
5889.951	Na I D <sub>2</sub>	1	absorption	a
5895.924	Na I D <sub>1</sub>	1	absorption	a
6102.723	Ca I	3	absorption	...
6122.217	Ca I	3	absorption	...
<i>inter-chip gap</i>				
6551.676	Fe I	13	absorption	...
6556.062	Ti I?	102	absorption	...
6572.779	Ca I	1	P-Cygni	...
6707.761	Li I	1	absorption	e,h
6707.912	Li I	1	absorption	e,h
7364.097	Ti I?	97	absorption	...
7698.974	K I	1	P-Cygni	...
7800.268	Rb I	1	P-Cygni	...
7947.603	Rb I	1	P-Cygni?	...

NOTE. — Photospheric signatures of the B3V companion are not included.

- a ISM feature
- b weak line; flux uncertain
- c Cs I 4555.8 Å resonance line?
- d absorption component very weak
- e blend
- f emission component weak
- g two separated components
- h P-Cygni profile?

TABLE 3  
 IDENTIFIED MOLECULAR BANDS

$\lambda_{\text{obs}}$ (Å)	$\lambda_{\text{lab}}$ (Å)	Molecule	Electronic transition	Feature	Vel. (km s <sup>-1</sup> )	Ref.	Notes
4420.5	4421.521	TiO	$\alpha$ (4,0)	R <sub>2</sub>		1	
4469.4	4470.54	AlO	B <sup>2</sup> $\Sigma^+$ – X <sup>2</sup> $\Sigma^+$ (2,0)	R		2	
4494.8	4494.04	AlO	B <sup>2</sup> $\Sigma^+$ – X <sup>2</sup> $\Sigma^+$ (3,1)	R		2	
4517.5	4516.40	AlO	B <sup>2</sup> $\Sigma^+$ – X <sup>2</sup> $\Sigma^+$ (4,2)	R		2	
4582.5	4584.056	TiO	$\alpha$ (3,0)	R <sub>2</sub>		1	
4624.8	4626.08	TiO	$\alpha$ (4,1)	R <sub>2</sub>		1	
4647.7	4648.23	AlO	B <sup>2</sup> $\Sigma^+$ – X <sup>2</sup> $\Sigma^+$ (1,0)	R		2	
4671.7	4672.02	AlO	B <sup>2</sup> $\Sigma^+$ – X <sup>2</sup> $\Sigma^+$ (2,1)	R		2	
4694.5	4694.62	AlO	B <sup>2</sup> $\Sigma^+$ – X <sup>2</sup> $\Sigma^+$ (3,2)	R		2	
4715.4	4715.54	AlO	B <sup>2</sup> $\Sigma^+$ – X <sup>2</sup> $\Sigma^+$ (4,3)	R		2	
4736.0	4735.82	AlO	B <sup>2</sup> $\Sigma^+$ – X <sup>2</sup> $\Sigma^+$ (5,4)	R		2	
4738.0	4737.460	TiO	c <sup>1</sup> $\Phi$ – X <sup>3</sup> $\Delta$ (0,0)	R <sub>13</sub>		2	
4754.4	4754.29	AlO	B <sup>2</sup> $\Sigma^+$ – X <sup>2</sup> $\Sigma^+$ (6,5)	R	+58 ± 10	2	
4757.9	4759.005	<sup>46</sup> Ti <sup>16</sup> O	$\alpha$ (2,0)	R <sub>2</sub>	-67 ± 6	3	a
4759.1	4759.973	<sup>47</sup> Ti <sup>16</sup> O	$\alpha$ (2,0)	R <sub>2</sub>		3	
...	4760.902	<sup>48</sup> Ti <sup>16</sup> O	$\alpha$ (2,0)	R <sub>2</sub>		3	
4803.0	4804.333	TiO	$\alpha$ (3,1)	R <sub>2</sub>		1	b
4840.95	4842.27	AlO	B <sup>2</sup> $\Sigma^+$ – X <sup>2</sup> $\Sigma^+$ (0,0)	R <sub>2</sub>	-82 ± 6	2	
4952.6	4954.562	TiO	$\alpha$ (1,0)	R <sub>2</sub>	-119 ± 6	1	
4997.9	4999.129	TiO	$\alpha$ (2,1)	R <sub>2</sub>		1	
5044.9	5044.501	TiO	$\alpha$ (3,2)	R <sub>2</sub>		4	
5078.0	5079.36	AlO	B <sup>2</sup> $\Sigma^+$ – X <sup>2</sup> $\Sigma^+$ (0,1)	R	-82 ± 6	2	
5100.7	5102.13	AlO	B <sup>2</sup> $\Sigma^+$ – X <sup>2</sup> $\Sigma^+$ (1,2)	R	-82 ± 6	2	
5122.0	5123.33	AlO	B <sup>2</sup> $\Sigma^+$ – X <sup>2</sup> $\Sigma^+$ (2,3)	R	-82 ± 6	5	
5143.7	5142.89	AlO	B <sup>2</sup> $\Sigma^+$ – X <sup>2</sup> $\Sigma^+$ (3,4)	R	+48 ± 12	2	
5161.8	5160.98	AlO	B <sup>2</sup> $\Sigma^+$ – X <sup>2</sup> $\Sigma^+$ (4,5)	R	+48 ± 12	2	
5164.6	5166.753	TiO	$\alpha$ (0,0)	R <sub>2</sub>	-125 ± 12	1	c
5227.4	5228.2	VO	C <sup>4</sup> $\Sigma^-$ – X <sup>4</sup> $\Sigma^-$ (2,0)	R <sub>4</sub>	-45 ± 12	2	
5276	5275.8	VO	C <sup>4</sup> $\Sigma^-$ – X <sup>4</sup> $\Sigma^-$ (3,1)			2	
5308.4	5307.337	TiO	$\alpha$ (3,3)	R <sub>2</sub>		4	
5312	5310.928	TiO	$\alpha$ (3,3)	R <sub>3</sub>		4	
5319.0	5319.746	TiO	$\gamma'$ (3,0)	R <sub>1</sub>		4	d
5320.4	5321.111	TiO	$\gamma'$ (3,0)	Q <sub>1</sub>		4	d
5338.6	5341.240	TiO	$\gamma'$ (3,0)	R <sub>2</sub>		4	d
5340.4	5343.223	TiO	$\gamma'$ (3,0)	Q <sub>2</sub>		4	d
5356.5	5355.975	TiO	$\alpha$ (4,4)	R <sub>2</sub>		4	
5361.5	5363.528	TiO	$\gamma'$ (3,0)	R <sub>3</sub>		4	d
5365.0	5367.167	TiO	$\gamma'$ (3,0)	Q <sub>3</sub>		4	d
...	5376.83	AlO	B <sup>2</sup> $\Sigma^+$ – X <sup>2</sup> $\Sigma^+$ (2,4)	R		2	
...	5411.960	TiO	$\gamma'$ (4,1)	R <sub>3</sub>		4	
...	5415.639	TiO	$\gamma'$ (4,1)	Q <sub>3</sub>		4	
5447.2	5448.233	TiO	$\alpha$ (0,1)	R <sub>2</sub>	-57 ± 18	1	
5467.9	5469.3	VO	C <sup>4</sup> $\Sigma^-$ – X <sup>4</sup> $\Sigma^-$ (1,0)	R <sub>4</sub>	-77 ± 12	2	
5497.7	5496.742	TiO	$\alpha$ (1,2)	R <sub>2</sub>	+55 ± 12	1	
5500.4	5499.741	TiO	$\alpha$ (1,2)	R <sub>3</sub>	+36 ± 12	1	
...	5517.3	VO	C <sup>4</sup> $\Sigma^-$ – X <sup>4</sup> $\Sigma^-$ (2,1)	R <sub>4</sub>		2	
...	5546.041	TiO	$\alpha$ (2,3)	R <sub>2</sub>		1	
5562.1	5562.130	TiO	$\gamma'$ (2,0)	<sup>S</sup> R <sub>21</sub>		5	
5568.9	5569.089	TiO	$\gamma'$ (2,0)	R <sub>1</sub>		5	
5591.4	5592.609	TiO	$\gamma'$ (2,0)	R <sub>2</sub>		5	
5616.4	5616.792	TiO	$\gamma'$ (2,0)	R <sub>3</sub>		5	
5640.3	5640.849	TiO	$\gamma'$ (3,1)	R <sub>2</sub>		5	
5662.0	5662.223	TiO	$\beta$ (2,2)	R		5	
5662.8, 5665.0	5665.19	TiO	$\gamma'$ (3,1)	R <sub>3</sub>		5	
5669.5	5669.966	TiO	$\gamma'$ (3,1)	Q <sub>3</sub>		5	
5688.5	5689.640	TiO	$\gamma'$ (4,2)	R <sub>2</sub>		5	
5691.3	5692.270	TiO	$\gamma'$ (4,2)	Q <sub>2</sub>		5	
5713.8	5714.805	TiO	$\gamma'$ (4,2)	R <sub>3</sub>		5	
5718.4	5719.223	TiO	$\gamma'$ (4,2)	Q <sub>3</sub>		5	
5735.2	5736.703	VO	C <sup>4</sup> $\Sigma^-$ – X <sup>4</sup> $\Sigma^-$ (0,0)	R <sub>4</sub>	-78 ± 6	2	
5759.4, 5760.4	5758.741	TiO	$\alpha$ (0,2)	R <sub>2</sub>		3	
5773.2	5772.74	ScO	A <sup>2</sup> $\Pi_{3/2}$ – X <sup>2</sup> $\Sigma^+$ (2,1)	<sup>R</sup> Q <sub>21</sub>		2	e
...	5811.60	ScO	A <sup>2</sup> $\Pi_{1/2}$ – X <sup>2</sup> $\Sigma^+$ (2,1)	Q <sub>1</sub>		2	e
5811.0	5809.872	TiO	$\alpha$ (1,3)	R <sub>2</sub>		3	
5827.7	5827.024	TiO	$\gamma'$ (1,0)	R <sub>31</sub>		3	
5837.3	5839.005	TiO	$\gamma'$ (1,0)	R <sub>21</sub>	-58 ± 10	3	
...	5847.593	TiO	$\gamma'$ (1,0)	R <sub>1</sub>		3	
5948.2	5947.680	TiO	$\gamma'$ (2,1)	R <sub>3</sub>		3	
5956.2	5954.419	TiO	$\gamma'$ (2,1)	Q <sub>3</sub>		3	
5972.5	5972.17	YO	A <sup>2</sup> $\Pi_{3/2}$ – X <sup>2</sup> $\Sigma^+$ (0,0)	<sup>R</sup> Q <sub>21</sub>	-8 ± 5	2	

TABLE 3 — *Continued*

$\lambda_{\text{obs}}$ (Å)	$\lambda_{\text{lab}}$ (Å)	Molecule	Electronic transition	Feature	Vel. (km s <sup>-1</sup> )	Ref.	Notes
5978.5	5977.433	TiO	$\gamma$ (3,0)	R <sub>3</sub>		3	
5980.8	...	YO	A <sup>2</sup> Π <sub>3/2</sub> - X <sup>2</sup> Σ <sup>+</sup> (0,0)		-8 ± 5	9	
5988.8	5987.72	YO	A <sup>2</sup> Π <sub>3/2</sub> - X <sup>2</sup> Σ <sup>+</sup> (1,1)	<sup>R</sup> Q <sub>21</sub>	+58 ± 5	2	
5999.2	6001.151	TiO	$\gamma$ (3,0)	R <sub>2</sub>		3	
6027.8	6028.184	TiO	$\gamma$ (3,0)	R <sub>1</sub>		3	
6034.4	6036.17	ScO	A <sup>2</sup> Π - X <sup>2</sup> Σ <sup>+</sup> (0,0)	<sup>R</sup> Q <sub>2G</sub> + <sup>R</sup> R <sub>2G</sub>	-55 ± 10	2	
...	6036.684	TiO	$\gamma$ (4,1)	R <sub>3</sub>		3	
6061.9	6060.782	TiO	$\gamma$ (4,1)	R <sub>2</sub>	+55 ± 5	5	
6065.2	6064.31	ScO	A <sup>2</sup> Π - X <sup>2</sup> Σ <sup>+</sup> (0,0)	<sup>R</sup> R <sub>1G</sub>	+45 ± 10	2	
...	6072.65	ScO	A <sup>2</sup> Π - X <sup>2</sup> Σ <sup>+</sup> (1,1)	<sup>R</sup> Q <sub>2G</sub>		2	
6077.5	6079.30	ScO	A <sup>2</sup> Π - X <sup>2</sup> Σ <sup>+</sup> (0,0)	<sup>Q</sup> Q <sub>1G</sub> + <sup>Q</sup> R <sub>1G</sub>	-55 ± 10	2	
...	6088.245	TiO	$\gamma$ (4,1)	R <sub>1</sub>		3	
6116.0	6115.97	ScO	A <sup>2</sup> Π - X <sup>2</sup> Σ <sup>+</sup> (1,1)	<sup>Q</sup> Q <sub>1G</sub> + <sup>Q</sup> R <sub>1G</sub>		2	
6130.8	6132.097	YO	A <sup>2</sup> Π <sub>1/2</sub> - X <sup>2</sup> Σ <sup>+</sup> (0,0)	<sup>R</sup> Q <sub>21</sub>		9	
6135.0	6134.472	TiO	$\gamma'$ (0,0)	<sup>T</sup> R <sub>31</sub>		3	
6144.5	...	TiO	$\gamma'$ (0,0)	<sup>S</sup> Q <sub>31</sub>			
6146.9	6148.68	TiO	$\gamma'$ (0,0)	<sup>S</sup> R <sub>21</sub>	-90 ± 10	6	
6157.1	6158.52	TiO	$\gamma'$ (0,0)	R <sub>1</sub>		6	
6185.1	6186.32	TiO	$\gamma'$ (0,0)	R <sub>2</sub>		6	
...	6189.65	TiO	$\gamma'$ (0,0)	Q <sub>2</sub>		6	
6213.4	6214.93	TiO	$\gamma'$ (0,0)	R <sub>3</sub>		6	
6220.9	6222.26	TiO	$\gamma'$ (0,0)	Q <sub>3</sub>	-70 ± 10	6	
6269.2	6268.86	TiO	$\gamma'$ (1,1)	R <sub>3</sub>	0 ± 15	5	
6276.3	6276.03	TiO	$\gamma'$ (1,1)	Q <sub>3</sub>	0 ± 15	5	
6293.2	6294.80	TiO	$\gamma$ (2,0)	R <sub>3</sub>		5	
6319.4	6321.21	TiO	$\gamma$ (2,0)	R <sub>2</sub>	-77 ± 5	5	
6349.5	6351.29	TiO	$\gamma$ (2,0)	R <sub>1</sub>	-80 ± 5	5	
...	6357.33	TiO	$\gamma$ (3,1)	R <sub>3</sub>		5	
6384.5	6384.18	TiO	$\gamma$ (3,1)	R <sub>2</sub>	+58 ± 5	5	
6410.2	6408.26	ScO	A <sup>2</sup> Π <sub>3/2</sub> - X <sup>2</sup> Σ <sup>+</sup> (0,1)	<sup>R</sup> Q <sub>2G</sub> + <sup>R</sup> R <sub>2G</sub>		2	f
6415.1	6414.75	TiO	$\gamma$ (3,1)	R <sub>1</sub>	+58 ± 5	5	
6459.6	6457.78	ScO	A <sup>2</sup> Π <sub>1/2</sub> - X <sup>2</sup> Σ <sup>+</sup> (0,1)	<sup>Q</sup> Q <sub>1G</sub> + <sup>Q</sup> R <sub>1G</sub>		2	f
6448.9	...	TiO	$\gamma$ (4,2)	R <sub>2</sub>			
6649.3	6651.271	TiO	$\gamma$ (1,0)	R <sub>3</sub>		1	
6679.1	6680.796	TiO	$\gamma$ (1,0)	R <sub>2</sub>		1	
6712.5	6714.477	TiO	$\gamma$ (1,0)	R <sub>1</sub>		1	
...	6717.599	TiO	$\gamma$ (2,1)	R <sub>3</sub>		1	
6747.0	6747.613	TiO	$\gamma$ (2,1)	R <sub>2</sub>		1	
6781.1	6781.815	TiO	$\gamma$ (2,1)	R <sub>1</sub>		1	
...	6784.560	TiO	$\gamma$ (3,2)	R <sub>3</sub>		1	
6815.9	6815.139	TiO	$\gamma$ (3,2)	R <sub>2</sub>		1	
6832.2	6832.596	TiO	b <sup>1</sup> Π - X <sup>3</sup> Δ	R	-82 ± 8	3	g
6838.9	6838	TiO	b <sup>1</sup> Π - X <sup>3</sup> Δ	Q,P		3	
6849.9	6849.927	TiO	$\gamma$ (3,2)	R <sub>1</sub>		1	
6884.3	6885.25	VO	B <sup>4</sup> Π - X <sup>4</sup> Σ <sup>-</sup> (2,0)	<sup>T</sup> R <sub>42</sub>		2	
6892.0	6893.86	VO	B <sup>4</sup> Π - X <sup>4</sup> Σ <sup>-</sup> (2,0)	<sup>S</sup> Q <sub>42</sub>		2	
6935.8	6937.	VO	B <sup>4</sup> Π - X <sup>4</sup> Σ <sup>-</sup> (2,0)				
6950.9	6952.39	VO	B <sup>4</sup> Π - X <sup>4</sup> Σ <sup>-</sup> (2,0)				
6977.9	6978.51	VO	B <sup>4</sup> Π - X <sup>4</sup> Σ <sup>-</sup> (2,0)				
6986.6	6985.59	VO	B <sup>4</sup> Π - X <sup>4</sup> Σ <sup>-</sup> (2,0)				
7003.5	7003.40	TiO	$\gamma$ (0,0)	<sup>S</sup> R <sub>32</sub>		4	
7037.8	7038.28	TiO	$\gamma$ (0,0)	<sup>S</sup> R <sub>21</sub>		4	
...	7054.256	TiO	$\gamma$ (0,0)	R <sub>3</sub>		1	
7085.5	7087.566	TiO	$\gamma$ (0,0)	R <sub>2</sub>		1	
...	7124.930	TiO	$\gamma$ (1,1)	R <sub>3</sub>		1	
7123.4	7125.510	TiO	$\gamma$ (0,0)	R <sub>1</sub>		1	
...	7158.850	TiO	$\gamma$ (1,1)	R <sub>2</sub>		1	
7231.8	7230.774	TiO	$\gamma$ (2,2)	R <sub>2</sub>		3	
7270.9	7269.985	TiO	$\gamma$ (2,2)	R <sub>1</sub>		3	
7332.5	7333.93	VO	B <sup>4</sup> Π - X <sup>4</sup> Σ <sup>-</sup> (1,0)	<sup>T</sup> R <sub>42</sub>	-60 ± 8	7	h
7371.5	7372.70	VO	B <sup>4</sup> Π - X <sup>4</sup> Σ <sup>-</sup> (1,0)	<sup>S</sup> Q <sub>31</sub>	-60 ± 8	7	h
...	7381.70	VO	B <sup>4</sup> Π - X <sup>4</sup> Σ <sup>-</sup> (1,0)	<sup>R</sup> P <sub>31</sub>		7	
...	7393.34	VO	B <sup>4</sup> Π - X <sup>4</sup> Σ <sup>-</sup> (1,0)	<sup>S</sup> R <sub>21</sub>		7	
...	7405	VO	B <sup>4</sup> Π - X <sup>4</sup> Σ <sup>-</sup> (1,0)			7	
...	7416.13	VO	B <sup>4</sup> Π - X <sup>4</sup> Σ <sup>-</sup> (1,0)	<sup>Q</sup> P <sub>21</sub>		7	
...	7433.79	VO	B <sup>4</sup> Π - X <sup>4</sup> Σ <sup>-</sup> (1,0)	R <sub>1</sub>		7	
...	7442.9	VO	B <sup>4</sup> Π - X <sup>4</sup> Σ <sup>-</sup> (1,0)			7	
7453.8	7455.2	VO	B <sup>4</sup> Π - X <sup>4</sup> Σ <sup>-</sup> (1,0)			7	
...	7474	VO	B <sup>4</sup> Π - X <sup>4</sup> Σ <sup>-</sup> (2,1)		+58 ± 8	7	h
7589.8	7589.284	TiO	$\gamma$ (0,1)	R <sub>3</sub>		1	

TABLE 3 — *Continued*

$\lambda_{\text{obs}}$ (Å)	$\lambda_{\text{lab}}$ (Å)	Molecule	Electronic transition	Feature	Vel. (km s <sup>-1</sup> )	Ref.	Notes
7627.5	7627.799	TiO	$\gamma$ (0,1)	R <sub>2</sub>		1	
7704.2	7704.997	TiO	$\gamma$ (1,2)	R <sub>2</sub>		1	
7744.4	7743.056	TiO	$\gamma$ (2,3)	R <sub>3</sub>		1	
7750.9	7749.487	TiO	$\gamma$ (1,2)	R <sub>1</sub>		1	
7783.8	7782.854	TiO	$\gamma$ (2,3)	R <sub>2</sub>		1	
7863.20	7865.29	VO	B <sup>4</sup> Π – X <sup>4</sup> Σ <sup>-</sup> (0,0)	<sup>S</sup> Q <sub>42</sub>	-80 ± 4	8	h
7894.20	7896.38	VO	B <sup>4</sup> Π – X <sup>4</sup> Σ <sup>-</sup> (0,0)	<sup>S</sup> Q <sub>31</sub>	-80 ± 4	8	h
7905.72	7907.80	VO	B <sup>4</sup> Π – X <sup>4</sup> Σ <sup>-</sup> (0,0)	<sup>R</sup> P <sub>31</sub>	-80 ± 4	8	h
...	7919.12	VO	B <sup>4</sup> Π – X <sup>4</sup> Σ <sup>-</sup> (0,0)	<sup>S</sup> R <sub>21</sub>		8	
7937.55	7939.62	VO	B <sup>4</sup> Π – X <sup>4</sup> Σ <sup>-</sup> (0,0)	R <sub>2</sub>	-80 ± 4	8	h
...	7950.29	VO	B <sup>4</sup> Π – X <sup>4</sup> Σ <sup>-</sup> (0,0)	<sup>Q</sup> R <sub>23</sub>		8	

REFERENCES. — (1) Phillips (1973); (2) Kopp et al. (1974); (3) Schwenke (1998); (4) Plez (1998); (5) Jørgensen (1994); (6) Hocking et al. (1979); (7) Cheung et al. (1994); (8) Adam et al. (1995); (9) Bernard & Gravina (1983).

<sup>a</sup> After correcting the laboratory wavelength from Phillips (1973) for the isotopic shift, as found from data in Schwenke (1998), one gets for the isotopomer <sup>46</sup>TiO the predicted stationary wavelength of 4759.205 Å and the velocity of -80 km s<sup>-1</sup>.

<sup>b</sup> The bandhead is strongly contaminated by the rotational structure of the  $\alpha$  (2,0) band of TiO in the range 4793–4803 Å.

<sup>c</sup> The bandhead is blended with two Fe I absorption lines at 5166.286 Å and 5168.901 Å. However, the blue edge of the blend should be formed by molecular absorption. The velocity given in the table is for the <sup>46</sup>TiO isotopomer (laboratory wavelength concluded from Schwenke 1998).

<sup>d</sup> All databases give different laboratory wavelengths.

<sup>e</sup> The band is probably contaminated by the A<sup>2</sup>Π<sub>1/2</sub>–X<sup>2</sup>Σ<sup>+</sup> (1,0) Q<sub>1</sub> feature of ScO.

<sup>f</sup> In emission.

<sup>g</sup> Velocity determined in simulations, see Fig. 14 for details.

<sup>h</sup> In the table the velocity of the blueshifted component of VO is given. The fit to all features of the VO (1,0) and (0,0) bands indicates a velocity of -2 km s<sup>-1</sup>.